



# Calculation of predictions for non-identical particle correlations in heavy ions collisions at LHC energies from hydrodynamics-inspired models

MASTER OF SCIENCE THESIS

Author:  
**Mateusz Wojciech Gałażyn**

Supervisor:  
**Prof. Adam Kisiel**

Warsaw, 2nd December 2014



# Wyznaczenie przewidywań teoretycznych dla korelacji cząstek nieidentycznych w zderzeniach ciężkich jonów przy energiach LHC w modelach opartych na hydrodynamice

PRACA MAGISTERSKA

Autor:  
**Mateusz Wojciech Gałażyn**

Promotor:  
**dr hab. inż. Adam Kisiel, prof. PW**

Warszawa, 2 grudnia 2014

## 1 Abstract

2 This thesis presents results of two-particle momentum correlations analysis  
3 for different kinds of particles produced in heavy ion collisions. The studies  
4 were carried for the data from lead-lead collisions at the centre of mass energy  
5  $\sqrt{s_{NN}} = 2.76$  TeV simulated in the THERMINATOR model using the (3+1)-  
6 dimensional hydrodynamic model with viscosity. Analysis was performed for  
7 the three particle kinds: pions, kaons and protons for the collisions in eight dif-  
8 ferent centrality ranges.

9 The THERMINATOR model allows to perform statistical hadronization of  
10 stable particles and unstable resonances from a given hypersurface which is  
11 followed by the resonance propagation and decay phase. The four-dimensional  
12 hypersurface is coming from the calculations performed on a basis of relativistic  
13 hydrodynamic framework with the viscosity corrections.

14 One can investigate space-time characteristics of the particle-emitting source  
15 through two-particle interferometry using experimental observables. The  
16 experimental-like analysis of the data coming from a model calculations yields  
17 a possibility to test the hydrodynamic description of a quark-gluon plasma.  
18 This thesis concentrates on the verification of the prediction of appearance of  
19 femtoscopic radii scaling with the transverse mass.

20 The three dimensional correlation functions were calculated using spherical  
21 harmonics decomposition. One can use this approach to perform calculations  
22 with lower statistics and moreover the visualization of results is much easier. The  
23 calculated correlation functions show expected increase of a correlation for pions  
24 and kaons at the low relative momenta of a pair. For the protons at the same mo-  
25 mentum region, the decrease occurs. The transverse pair momentum and cen-  
26 trality dependence on a correlation function is observed. In order to perform the  
27 quantitative analysis of this influence, the fitting of theoretical formula for cor-  
28 relation function was performed. The femtoscopic radii calculated in the LCMS  
29 and PRF are falling with the transverse mass  $m_T$ . To test the scaling predicted  
30 from the hydrodynamics, the power law was fitted  $\alpha m_T^{-\beta}$ . The radii calculated  
31 for pions, kaons and protons in the LCMS are following the common scaling. In  
32 case of the PRF no such scaling is observed. To recover the scaling in the PRF, the  
33 approximate factor is proposed:  $\sqrt{(\sqrt{\gamma_T} + 2)/3}$ . The radii in the PRF divided by  
34 the proposed scaling factor are falling on the common curve, therefore the scaling  
35 can be recovered using the proposed scaling factor. The experimental analysis is  
36 usually performed in the PRF (requires less statistics), hence the method of scal-  
37 ing recovery enables easier testing of the hydrodynamic predictions, which are  
38 not visible in the PRF.

## Streszczenie

40 W tej pracy zaprezentowane są wyniki analizy dwucząstkowych korelacji pę-  
 41 dowych dla trzech różnych typów cząstek produkowanych w zderzeniach cięż-  
 42 kich jonów. Obliczenia zostały wykonane dla danych ze zderzeń ołów-ołów przy  
 43 energii w centrum masy  $\sqrt{s_{NN}} = 2.76$  TeV wygenerowanych za pomocą mo-  
 44 delu THERMINATOR przy użyciu (3+1)-wymiarowego modelu hydrodynamicz-  
 45 nego uwzględniającego lepkość ośrodka. Analiza została wykonana dla trzech  
 46 rodzajów cząstek: pionów, kaonów i protonów dla dziewięciu różnych przedzia-  
 47 łów centralności.

48 Model THERMINATOR pozwala na wykonanie statystycznej hadronizacji  
 49 stabilnych cząstek jak i również niestabilnych rezonansów z danej  
 50 hiperpowierzchni wymrażania, a następnie uwzględnienie propagacji i  
 51 rozpadów tych rezonansów. Czterowymiarowa hiperpowierzchnia pochodzi z  
 52 obliczeń przeprowadzonych na podstawie hydrodynamiki relatywistycznej z  
 53 uwzględnieniem poprawek pochodzących od lepkości.

54 Interferometria dwucząstkowa pozwala na zbadanie charakterystyk  
 55 czasowo-przestrzennych źródła cząstek. Poprzez analizę danych pochodzących  
 56 z obliczeń modelowych można dokonać sprawdzenia zakresu stosownalności  
 57 hydrodynamiki do opisu właściwości plazmy kwarkowo-gluonowej. Ta praca  
 58 koncentruje się na weryfikacji skalowania promieni femtoskopowych z masą  
 59 poprzeczną przewidywanego przez hydrodynamikę.

60 Trójwymiarowe funkcje korelacyjne zostały obliczone za pomocą rozkładu w  
 61 szeregu harmonik sferycznych. To podejście wymaga mniejszej statystyki i po-  
 62zwala na łatwiejszą wizualizację wyników. Obliczone funkcje korelacyjne wy-  
 63kazują oczekiwany wzrost korelacji dla niskich różnic pędów dla par pionów i  
 64 kaonów. Dla par protonów w tym samym zakresie pędów widoczny jest spa-  
 65dek korelacji. Widoczny jest wpływ pędu poprzecznego pary oraz centralności  
 66 na funkcję korelacyjną. W celu wykonania analizy ilościowej tego wpływu, zo-  
 67stało wykonane dopasowanie formuły analitycznej do obliczonych funkcji kore-  
 68lacyjnych. Otrzymane w ten sposób promienie femtoskopowe w LCMS i PRF  
 69 wykazują spadek wraz z wzrostem masy poprzecznej  $m_T$ . W celu sprawdzenie  
 70 skalowania przewidywanego przez hydrodynamikę została dopasowana zależ-  
 71ność potęgowa:  $\alpha m_T^{-\beta}$ . Promienie obliczone dla pionów, kaonów i protonów  
 72 zachowują wzajemne skalowanie w LCMS. W przypadku PRF skalowanie nie  
 73 jest widoczne. Aby odzyskać skalowanie w PRF, został zaproponowany przy-  
 74 bliżony współczynnik:  $\sqrt{(\sqrt{\gamma_T} + 2)/3}$ . Promienie w PRF po podzieleniu przez

<sup>75</sup> współczynnik skalowania, są opisywalne przez podaną zależność potęgową, za-  
<sup>76</sup> tem umożliwia on odzyskanie skalowania. Analiza eksperimentalna jest zazwy-  
<sup>77</sup> czaj wykonywana w PRF (wymaga mniejszej statystyki), zatem ta metoda po-  
<sup>78</sup> zwala na łatwiejszą weryfikację przewidywań hydrodynamiki które są widoczne  
<sup>79</sup> w LCMS, a nie są w PRF.

# <sup>80</sup> Contents

<sup>81</sup>	<b>Introduction</b>	<b>1</b>
<sup>82</sup>	<b>1 Theory of heavy ion collisions</b>	<b>3</b>
<sup>83</sup>	1.1 The Standard Model . . . . .	3
<sup>84</sup>	1.2 Quantum Chromodynamics . . . . .	4
<sup>85</sup>	1.2.1 Quarks and gluons . . . . .	4
<sup>86</sup>	1.2.2 Quantum Chromodynamics potential . . . . .	5
<sup>87</sup>	1.2.3 The quark-gluon plasma . . . . .	7
<sup>88</sup>	1.3 Relativistic heavy ion collisions . . . . .	9
<sup>89</sup>	1.3.1 Stages of heavy ion collision . . . . .	9
<sup>90</sup>	1.3.2 QGP signatures . . . . .	11
<sup>91</sup>	<b>2 Therminator model</b>	<b>19</b>
<sup>92</sup>	2.1 (3+1)-dimensional viscous hydrodynamics . . . . .	19
<sup>93</sup>	2.2 Statistical hadronization . . . . .	20
<sup>94</sup>	2.2.1 Cooper-Frye formalism . . . . .	21
<sup>95</sup>	2.3 Events generation procedure . . . . .	22
<sup>96</sup>	<b>3 Particle interferometry</b>	<b>25</b>
<sup>97</sup>	3.1 HBT interferometry . . . . .	25
<sup>98</sup>	3.2 Theoretical approach . . . . .	25
<sup>99</sup>	3.2.1 Conventions used . . . . .	26
<sup>100</sup>	3.2.2 Two particle wave function . . . . .	27
<sup>101</sup>	3.2.3 Source emission function . . . . .	28
<sup>102</sup>	3.2.4 Analytical form of a correlation function . . . . .	30
<sup>103</sup>	3.2.5 Spherical harmonics decomposition of a correlation function	31
<sup>104</sup>	3.3 Experimental approach . . . . .	32
<sup>105</sup>	3.4 Scaling of femtoscopic radii . . . . .	33
<sup>106</sup>	3.4.1 Scaling in LCMS . . . . .	34
<sup>107</sup>	3.4.2 Scaling in PRF . . . . .	35
<sup>108</sup>	<b>4 Results</b>	<b>36</b>
<sup>109</sup>	4.1 Identical particles correlations . . . . .	36
<sup>110</sup>	4.1.1 Spherical harmonics components . . . . .	36

111	4.1.2	Centrality dependence of a correlation function . . . . .	40
112	4.1.3	$k_T$ dependence of a correlation function . . . . .	41
113	4.2	Results of the fitting procedure . . . . .	42
114	4.2.1	The three-dimensional femtoscopic radii scaling . . . . .	42
115	4.2.2	Scaling of one-dimensional radii . . . . .	46
116	4.3	Discussion of the results . . . . .	47
117	<b>Conclusions</b>		<b>48</b>
118	<b>A Scripts for correlation function calculations</b>		<b>50</b>
119	A.1	Events generation . . . . .	50
120	A.2	Calculations of experimental-like correlation functions . . . . .	51
121	<b>B Fitting utilities</b>		<b>52</b>
122	B.1	Minuit package . . . . .	52
123	B.2	Fitting software . . . . .	52
124	B.2.1	Input parameters . . . . .	52
125	B.2.2	Output format . . . . .	54
126	B.2.3	Compilation . . . . .	54
127	B.2.4	Usage . . . . .	54
128	<b>C Plotting scripts</b>		<b>55</b>

# <sup>129</sup> Introduction

Many people were trying to discover what was in the beginning of the Universe which we observe today. Through the years, more or less successful theories were appearing and trying to describe its origin and behaviour. Among them is one model, which provides a comprehensive explanation for a broad range of phenomena, including the cosmic microwave background, abundance of the light elements and Hubble's law. This model is called The Big Bang theory and has been born in 1927 on the basis of principles proposed by the Belgian priest and scientist Georges Lemaître. Using this model and known laws of physics one can calculate the characteristics of the Universe in detail back in time to the extreme densities and temperatures. However, at some point these calculations fail. The extrapolation of the expansion of the Universe backwards in time using general relativity yields an infinite density and temperature at a finite time in the past. This appearance of singularity is a signal of the breakdown of general relativity. The range of this extrapolation towards singularity is debated - certainly we can go no closer than the end of *Planck epoch* i.e.  $10^{-43}$  s. At this very first era the temperature of the Universe was so high, that the four fundamental forces - electromagnetism, gravitation, weak nuclear interaction and strong nuclear interaction - were one fundamental force. Between  $10^{-43}$  s and  $10^{-36}$  s of a lifetime of the Universe, there is a *grand unification epoch*, at which forces are starting to separate from each other. The *electroweak epoch* lasted from  $10^{-36}$  s to  $10^{-12}$  s, when the strong force separated from the electroweak force. After the electroweak epoch, there was the *quark epoch* in which the Universe was a dense "soup" of quarks. During this stage the fundamental forces of gravitation, electromagnetism, strong and weak interactions had taken their present forms. The temperature at this moment was still too high to allow quarks to bind together and form hadrons. At the end of quark era, there was a big freeze-out - when the average energy of particle interactions had fallen below the binding energy of hadrons. This era, in which quarks became confined into hadrons, is known as the *hadron epoch*. At this moment the matter had started forming nuclei and atoms, which we observe today.

Here arises the question: how can we study the very beginning of the Universe? To do this, one should create in a laboratory a system with such a large density and high temperature to recreate those conditions. Today, this is achievable through sophisticated machines, which are particle accelerators. In

164 the particle accelerators, like the Large Hadron Collider at CERN, Geneva or  
165 Relativistic Heavy Ion Collider at Brookhaven National Laboratory in Upton,  
166 New York, the heavy ions after being accelerated to near the speed of light are  
167 collided in order to generate extremely dense and hot phase of matter and  
168 recreate the quark-gluon plasma. The plasma is believed to behave like an  
169 almost ideal fluid and to become a medium, that can be described by the laws of  
170 relativistic hydrodynamics.

171 This thesis is providing predictions for collective behaviour of the quark-  
172 gluon plasma coming from the hydrodynamic equations. Experimental-like  
173 analysis was performed for the high energy Pb-Pb collisions generated with  
174 THERMINATOR model.

175 The 1st chapter is an introduction to the theory of heavy ion collisions. It  
176 contains the brief description of the Standard Model and Quantum Chromody-  
177 namics. The quark-gluon plasma and its signatures are also characterized.

178 In the 2nd chapter, the relativistic hydrodynamic framework and the  
179 THERMINATOR model used to perform the simulations of collisions are  
180 characterized.

181 The 3rd chapter covers the particle interferometry method used in this  
182 work. The effects coming from the hydrodynamics in the experimental results  
183 for particle interferometry are also presented. An algorithm of building  
184 experimental correlation functions is also described in this chapter.

185 In the 4th chapter, a detailed analysis of the results for two-particle femto-  
186 scopy for different pairs of particles is presented. The quantitative analysis of  
187 calculated femtoscopic radii as well as the appearance of transverse mass scaling  
188 is discussed.

<sup>189</sup> **Chapter 1**

<sup>190</sup> **Theory of heavy ion collisions**

<sup>191</sup> **1.1 The Standard Model**

<sup>192</sup> In the 1970s, a new theory of fundamental particles and their interaction  
<sup>193</sup> emerged. It was a new concept, which combines the electromagnetic, weak and  
<sup>194</sup> strong nuclear interactions between known particles. This theory is called *The*  
<sup>195</sup> *Standard Model*. There are seventeen named particles in the standard model, or-  
<sup>196</sup> ganized into the chart shown below (Fig. 1.1). Fundamental particles are divided  
into two families: *fermions* and *bosons*.

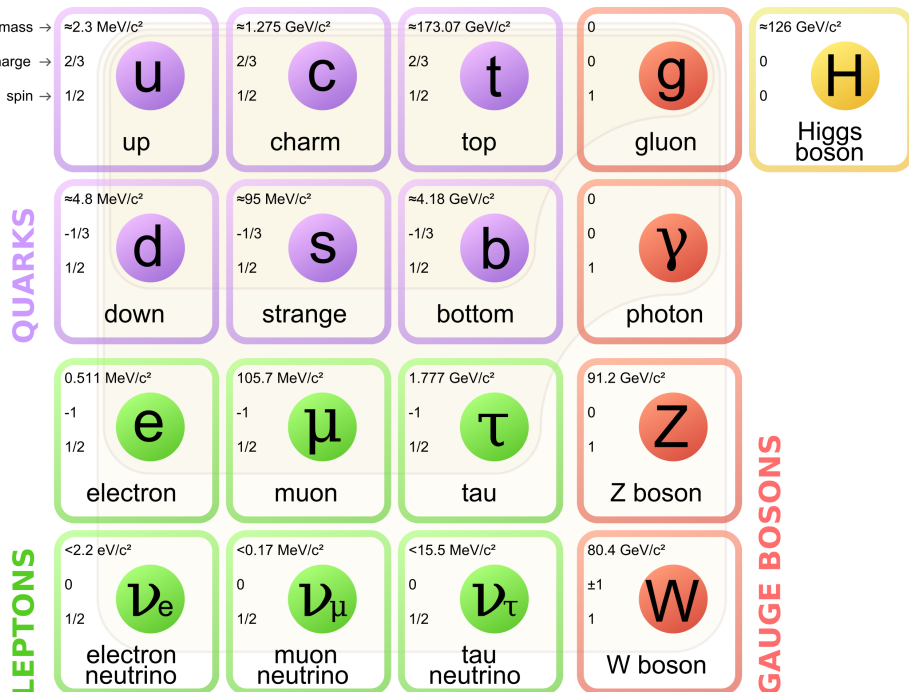


Figure 1.1: The Standard Model of elementary particles [1].

197 Fermions are the building blocks of matter. They are divided into two groups.  
 198 Six of them, which must bind together are called *quarks*. Quarks are known to  
 199 bind into doublets (*mesons*), triplets (*baryons*) and recently confirmed four-quark  
 200 states<sup>1</sup>. Two of baryons, with the longest lifetimes, are forming a nucleus: a pro-  
 201 ton and a neutron. A proton is build from two up quarks and one down, and  
 202 neutron consists of two down quarks and one up. A proton is found to be a stable  
 203 particle (at least it has a lifetime larger than  $10^{35}$  years) while a free neutron has a  
 204 mean lifetime about  $8.8 \times 10^2$  s. Fermions that can exist independently are called  
 205 *leptons*. Neutrinos are a subgroup of leptons, which are only influenced by weak  
 206 interaction. Fermions can be divided into three generations (three columns in  
 207 the Figure 1.1). Generation I particles can combine into hadrons with the longest  
 208 life spans. Generation II and III consists of unstable particles which also form  
 209 unstable hadrons.

210 Bosons are force carriers. There are four fundamental forces: weak - respons-  
 211 ible for radioactive decay, strong - coupling quarks into hadrons, electromagnetic  
 212 - between charged particles and gravity - the weakest, which causes the attraction  
 213 between particles with mass. The Standard Model describes the first three. The  
 214 weak force is mediated by  $W^\pm$  and  $Z^0$  bosons, electromagnetic force is carried by  
 215 photons  $\gamma$  and the carriers of a strong interaction are gluons  $g$ . The fifth boson is  
 216 a Higgs boson which is responsible for giving other particles mass.

## 217 1.2 Quantum Chromodynamics

### 218 1.2.1 Quarks and gluons

219 Quarks interact with each other through the strong interaction. The medi-  
 220 ator of this force is a *gluon* - a massless and electrical chargeless particle. In the  
 221 quantum chromodynamics (QCD) - theory describing strong interaction - there  
 222 are six types of "charges" (like electrical charges in the electrodynamics) called  
 223 *colours*. The colours were introduced because some of the observed particles, like  
 224  $\Delta^-$ ,  $\Delta^{++}$  and  $\Omega^-$  appeared to consist of three quarks with the same flavour ( $ddd$ ,  
 225  $uuu$  and  $sss$  respectively), which was in conflict with the Pauli principle. One  
 226 quark can carry one of the three colours (usually called *red*, *green* and *blue*) and anti-  
 227 quark one of the three anti-colours respectively. Only colour-neutral (or white)  
 228 particles could exist. Mesons are assumed to be a colour-anticolour pair, while  
 229 baryons are *red-green-blue* triplets. Gluons also are colour-charged and there are  
 230 8 types of gluons. Therefore they can interact with themselves [3].

---

<sup>1</sup>The LHCb experiment at CERN in Geneva confirmed recently the existence of  $Z(4430)$  - a particle consisting of four quarks [2].

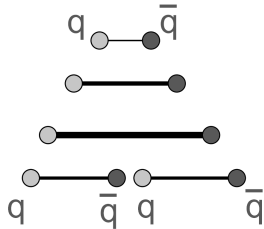
### 231 1.2.2 Quantum Chromodynamics potential

232 As a result of the fact that gluons are massless, one can expect, that the static  
 233 potential in QCD will have the form like similar one in electrodynamics e.g.  
 234  $\sim 1/r$  (by analogy to photons). In reality the QCD potential is assumed to have  
 235 the form of [3]

$$236 V_s = -\frac{4}{3} \frac{\alpha_s}{r} + kr, \quad (1.1)$$

236 where the  $\alpha_s$  is a coupling constant of the strong force and the  $kr$  part is related  
 237 with *confinement*. In comparison to the electromagnetic force, a value of the strong  
 238 coupling constant is  $\alpha_s \approx 1$  and the electromagnetic one is  $\alpha = 1/137$ .

239 The fact that quarks does not exist separately and are always bound, is called  
 240 confinement. As two quarks are pulled apart, the linear part  $kr$  in the Eq. 1.1  
 241 becomes dominant and the potential becomes proportional to the distance. This  
 242 situation resembles stretching of a string. At some point, when the string is so  
 243 large it is energetically favourable to create a quark-antiquark pair. At this  
 244 moment such pair (or pairs) is formed, the string breaks and the confinement is  
 preserved (Fig. 1.2).



245 Figure 1.2: A string breaking and a creation of a new quark-antiquark pair [4].

246 On the other hand, for small  $r$ , an interaction between the quarks and gluons  
 247 is dominated by the Coulomb-like term  $-\frac{4}{3} \frac{\alpha_s}{r}$ . The coupling constant  $\alpha_s$  depends  
 248 on the four-momentum  $Q^2$  transferred in the interaction. This dependence is  
 249 presented in Fig. 1.3. The value  $\alpha_s$  decreases with increasing momentum trans-  
 250 fer and the interaction becomes weak for large  $Q^2$ , i.e.  $\alpha_s(Q) \rightarrow 0$ . Because  
 251 of the weakening of coupling constant, quarks at large energies (or small dis-  
 252 tances) are starting to behave like free particles. This phenomenon is known as  
 253 *asymptotic freedom*. The QCD potential also has temperature dependence - the  
 254 force strength "melts" with the temperature increase. Therefore the asymptotic  
 255 freedom is expected to appear in either the case of high baryon densities (small  
 256 distances between quarks) or very high temperatures. This temperature depend-  
 257 ence is illustrated in Fig. 1.4.

258 If the coupling constant  $\alpha_s$  is small, one can use perturbative methods to cal-  
 259 culate physical observables. Perturbative QCD (pQCD) successfully describes  
 260 hard processes (with large  $Q^2$ ), such as jet production in high energy proton-  
 261 antiproton collisions. The applicability of pQCD is defined by the *scale parameter*



Figure 1.3: The coupling parameter  $\alpha_s$  dependence on four-momentum transfer  $Q^2$  [5].

262  $\Lambda_{QCD} \approx 200$  MeV. If  $Q \gg \Lambda_{QCD}$  then the process is in the perturbative domain  
 263 and can be described by pQCD. A description of soft processes (when  $Q < 1$  GeV)  
 264 is a problem in QCD - perturbative theory breaks down at this scale. Therefore,  
 265 to describe processes with low  $Q^2$ , one has to use alternative methods like Lattice  
 266 QCD. Lattice QCD (LQCD) is non-perturbative implementation of a field theory  
 267 in which QCD quantities are calculated on a discrete space-time grid. LQCD al-  
 268 lows to obtain properties of matter in equilibrium, but there are some limitations.  
 269 Lattice QCD requires fine lattice spacing to obtain precise results - therefore large  
 270 computational resources are necessary. With the constant growth of computing  
 271 power this problem will become less important. The second problem is that lat-  
 272 tice simulations are possible only for baryon density  $\mu_B = 0$ . At  $\mu_B \neq 0$ , Lattice  
 273 QCD breaks down because of the sign problem. In QCD the thermodynamic  
 274 observables are related to the grand canonical partition function, which has a ba-  
 275 ryonic chemical potential  $\mu_B$  as a parameter. Therefore, the baryonic density can  
 276 be controlled by tuning the baryonic chemical potential. For fermions  $\mu_B$  can be  
 277 both positive and negative. For a particles with  $\mu_B$ , their antiparticles have chem-  
 278 ical potentials with opposite sign  $-\mu_B$ . Since at the early universe the number of  
 279 baryons and antibaryons were almost equal we can use  $\mu_B = 0$  to a very good  
 280 approximation [6].

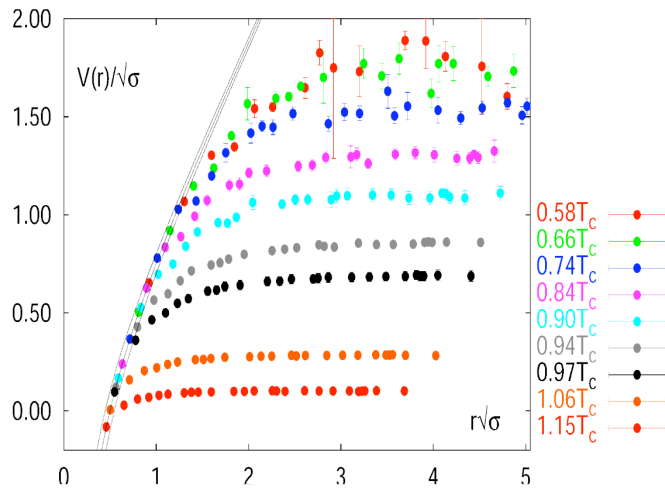


Figure 1.4: The QCD potential for a quark-antiquark pair as a function of distance for different temperatures. A value of a potential decreases with the temperature [4].

### 1.2.3 The quark-gluon plasma

The new state of matter in which quarks are no longer confined is known as a *quark-gluon plasma* (QGP). The predictions coming from the discrete space-time Lattice QCD calculations reveal a phase transition from the hadronic matter to the quark-gluon plasma at the high temperatures and baryon densities. The results obtained from such calculations are shown on Fig. 1.5. The energy density  $\epsilon$  which is divided by  $T^4$  is a measure of the number of degrees of freedom in

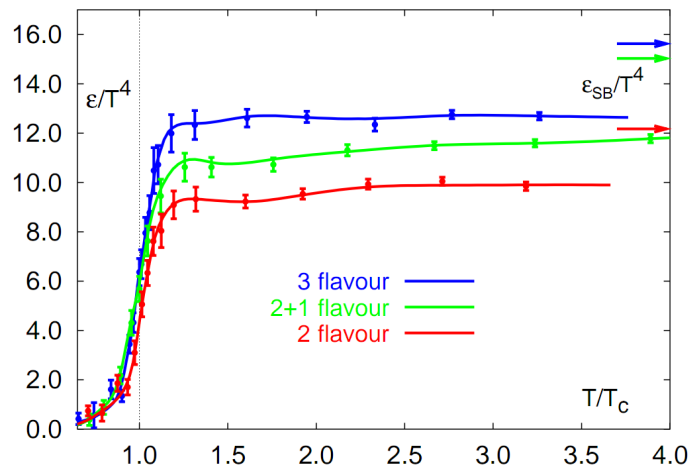


Figure 1.5: A number of degrees of freedom as a function of a temperature [7].

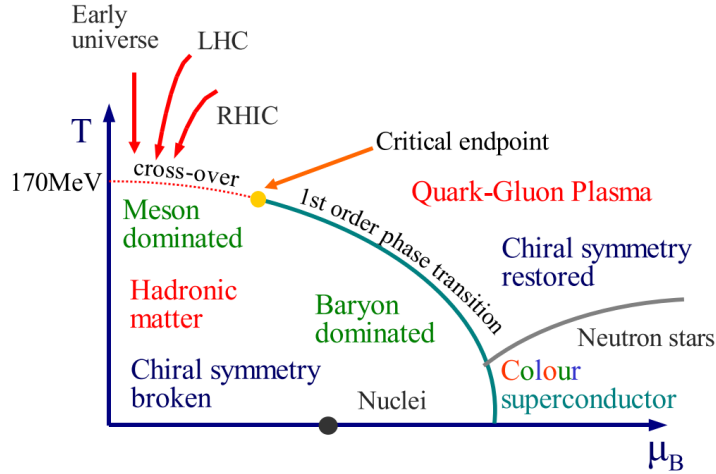


Figure 1.6: Phase diagram coming from the Lattice QCD calculations [8].

the system. One can observe significant rise of this value, when the temperature increases past the critical value  $T_C$ . Such increase is signaling a phase transition - the formation of QGP [8]. The values of the energy densities plotted in Fig. 1.5 do not reach the Stefan-Boltzmann limit  $\epsilon_{SB}$  (marked with arrows), which corresponds to an ideal gas. This can indicate some residual interactions in the system. According to the results from the RHIC<sup>2</sup>, the new phase of matter behaves more like an ideal fluid, than like a gas [9].

One of the key questions, to which current heavy ion physics tries to find an answer is the value of a critical temperature  $T_C$  as a function of a baryon chemical potential  $\mu_B$  (baryon density), where the phase transition occurs. The results coming from the Lattice QCD are presented in Fig. 1.6. The phase of matter in which quarks and gluons are deconfined is expected to exist at large temperatures. In the region of small temperatures and high baryon densities, a different state is supposed to appear - a *colour superconductor*. The phase transition between hadronic matter and the QGP is thought to be of 1<sup>st</sup> order at  $\mu_B \gg 0$ . However as  $\mu_B \rightarrow 0$  quarks' masses become significant and a sharp transition transforms into a rapid but smooth cross-over. It is believed that in Pb-Pb collisions observed at the LHC<sup>3</sup>, the created matter has high enough temperature to be in the quark-gluon plasma phase, then cools down and converts into hadrons, undergoing a smooth transition [8].

<sup>2</sup>Relativistic Heavy Ion Collider at Brookhaven National Laboratory in Upton, New York

<sup>3</sup>Large Hadron Collider at CERN, Geneva

### 308 1.3 Relativistic heavy ion collisions

#### 309 1.3.1 Stages of heavy ion collision

310 To create the quark-gluon plasma one has to achieve high enough temper-  
 311 atures and baryon densities. Such conditions can be recreated in the heavy ion  
 collisions at the high energies. The left side of the Figure 1.7 shows simplified

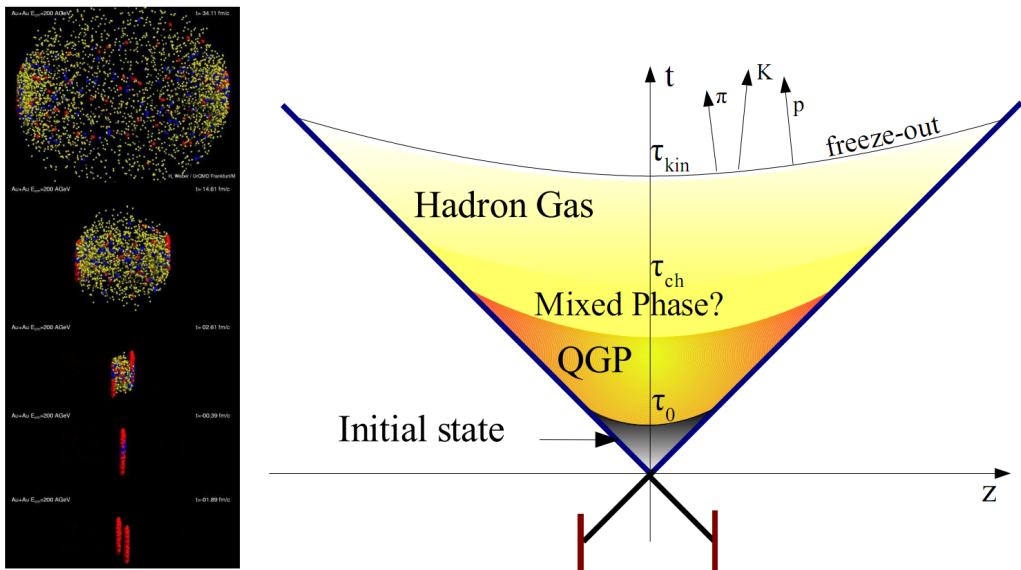


Figure 1.7: Left: stages of a heavy ion collision simulated in the UrQMD model.  
 Right: schematic view of a heavy ion collision evolution [8].

312 picture of a central collision of two highly relativistic nuclei in the centre-of-  
 313 mass reference frame. The colliding nuclei are presented as thin disks because  
 314 of the Lorentz contraction. In the central region, where the energy density is the  
 315 highest, a new state of matter - the quark-gluon plasma - is supposedly created.  
 316 Afterwards, the plasma expands and cools down, quarks combine into hadrons  
 317 and their mutual interactions cease when the system reaches the *freeze-out* tem-  
 318 perature. Subsequently, produced free hadrons move towards the detectors.  
 319

320 On the right side of the Figure 1.7 a space-time evolution of a collision process  
 321 is presented, plotted in the light-cone variables ( $z, t$ ). The two highly relativistic  
 322 nuclei are traveling basically along the light cone until they collide at the centre  
 323 of the diagram. Nuclear fragments emerge from the collision again along the  
 324 (forward) light cone, while the matter between fragmentation zones populates  
 325 the central region. This hot and dense matter is believed to be in the state of the  
 326 quark-gluon plasma. Several frameworks exist to describe this transition to the  
 327 QGP phase, for example: QCD string breaking, QCD parton cascades or colour  
 328 glass condensate evolving into glasma and later into quark-gluon plasma [10].

329 **String breaking** – In the string picture, the nuclei pass through each other forming colour strings. This is analogous to the situation depicted in the Fig 1.2 - the  
 330 colour string is created between quarks inside particular nucleons in nuclei. In  
 331 the next step strings decay / fragment forming quarks and gluons or directly  
 332 hadrons. This approach becomes invalid at very high energies, when the strings  
 333 overlap and cannot be treated as independent objects.

334 **Parton cascade** – The parton<sup>4</sup> cascade model is based on the pQCD. The colliding  
 335 nuclei are treated as clouds of quarks which penetrate through each other.  
 336 The key element of this method is the time evolution of the parton phase-space  
 337 distributions, which is governed by a relativistic Boltzmann equation with a col-  
 338 lision term that contains dominant perturbative QCD interactions. The bottleneck  
 339 of the parton cascade model is the low energies regime, where the  $Q^2$  is too small  
 340 to be described by the perturbative theory.

341 **Colour glass condensate** – The colour glass condensate assumes, that the had-  
 342 ion can be viewed as a tightly packed system of interacting gluons. The sat-  
 343 uration of gluons increases with energy, hence the total number of gluons may  
 344 increase without bound. Such a saturated and weakly coupled gluon system is  
 345 called a colour glass condensate. The fast gluons in the condensate are Lorentz  
 346 contracted and redistributed on the two very thin sheets representing two col-  
 347 liding nuclei. The sheets are perpendicular to the beam axis. The fast gluons  
 348 produce mutually orthogonal colour magnetic and electric fields, that only ex-  
 349 ist on the sheets. Immediately after the collision, i.e. just after the passage of  
 350 the two gluonic sheets through each other, the longitudinal electric and magnetic  
 351 fields are produced forming the *glasma*. The glasma fields decay through the  
 352 classical rearrangement of the fields into radiation of gluons. Also decays due to  
 353 the quantum pair creations are possible. In this way, the quark-gluon plasma is  
 354 produced.

355 Interactions within the created quark-gluon plasma bring the system into  
 356 the local statistical equilibrium, hence its further evolution can be described by  
 357 the relativistic hydrodynamics. The hydrodynamic expansion causes the sys-  
 358 tem to become more and more dilute. The phase transition from the quark-gluon  
 359 plasma to the hadronic gas occurs. Further expansion causes a transition from the  
 360 strongly interaction hadronic gas to weakly interacting system of hadrons which  
 361 move freely to the detectors. Such decoupling of hadrons is called the *freeze-out*.  
 362 The freeze-out can be divided into two phases: the chemical freeze-out and the  
 363 thermal one. The *chemical freeze-out* occurs when the inelastic collisions between  
 364 constituents of the hadron gas stop. As the system evolves from the chemical  
 365 freeze-out to the thermal freeze-out the dominant processes are elastic collisions  
 366 (such as, for example  $\pi + \pi \rightarrow \rho \rightarrow \pi + \pi$ ) and strong decays of heavier reso-  
 367 nances which populate the yield of stable hadrons. The *thermal freeze-out* is the  
 368 stage of the evolution of matter, when the strongly coupled system transforms  
 369 to a weakly coupled one (consisting of essentially free particles). In other words

---

<sup>4</sup>A parton is a common name for a quark and a gluon.

371 this is the moment, where the hadrons practically stop to interact. Obviously, the  
 372 temperatures corresponding to the two freeze-outs satisfy the condition

$$T_{chem} > T_{therm}, \quad (1.2)$$

373 where  $T_{chem}$  (inferred from the ratios of hadron multiplicities) is the temperature  
 374 of the chemical freeze-out, and  $T_{therm}$  (obtained from the investigation of the  
 375 transverse-momentum spectra) is the temperature of the thermal freeze-out [10].

### 376 1.3.2 QGP signatures

377 The quark-gluon plasma is a very short living and unstable state of matter.  
 378 One cannot investigate the properties of a plasma and confirm its existence directly.  
 379 Hence, the several experimental effects were proposed as QGP signatures,  
 380 some of them have been already observed in heavy ion experiments [8]. As matter  
 381 created in the heavy ions collisions is supposed to behave like a fluid, one  
 382 should expect appearance of collective behaviour at small transverse momenta  
 383 - so called *elliptic flow* and *radial flow*. The next signal is the temperature range  
 384 obtained from the measurements of *direct photons*, which gives us information,  
 385 that the system created in heavy ion collisions is far above the critical temperature  
 386 obtained from the LQCD calculations. The *puzzle in the di-lepton spectrum* can  
 387 be explained by the modification of spectral shape of vector mesons (mostly  $\rho$   
 388 meson) in the presence of a dense medium. This presence of a medium can also  
 389 shed light on the *jet quenching* phenomenon - the suppression occurrence in the  
 390 high  $p_T$  domain.

#### 391 Elliptic flow

392 In a non-central heavy ion collisions, created region of matter has an almond  
 393 shape with its shorter axis in the *reaction plane* (Fig. 1.8). The pressure gradient

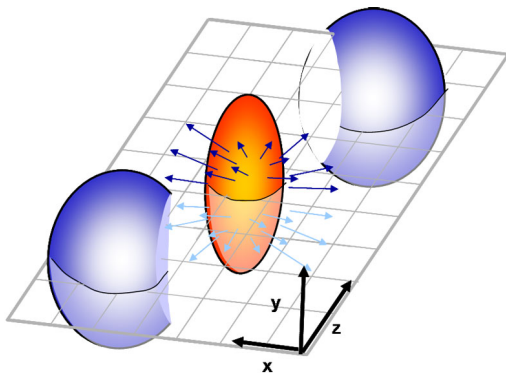


Figure 1.8: Overlapping region which is created in heavy ion collisions has an almond shape. Visible x-z plane is a *reaction plane*. The x-y plane is a *transverse plane*. The z is a direction of the beam [11].

394 is much larger in-plane rather than out-of-plane. This causes larger acceleration  
 395 and transverse velocities in-plane rather than out-of-plane. Such differences can  
 396 be investigated by studying the distribution of particles with respect to the reac-  
 397 tion plane orientation [12]:

$$E \frac{d^3 N}{dp^3} = \frac{1}{2\pi} \frac{d^2 N}{p_T dp_T dy} (1 + 2v_1 \cos(\phi) + 2v_2 \cos(2\phi) + \dots), \quad (1.3)$$

398 where  $\phi$  is the angle between particle transverse momentum  $p_T$  (a momentum  
 399 projection on a transverse plane) and the reaction plane,  $N$  is a number of  
 400 particles and  $E$  is an energy of a particle. The  $y$  variable is *rapidity* defined as:

$$y = \frac{1}{2} \ln \left( \frac{E + p_L}{E - p_L} \right), \quad (1.4)$$

401 where  $p_L$  is a longitudinal component of a momentum (parallel to the beam direc-  
 402 tion). The  $v_n$  coefficients indicate the shape of a system. For the most central col-  
 403 lisions ( $b = 0$  - see Fig. 1.9) all coefficients vanish  $\sum_{n \in N_+} v_n = 0$  (the overlapping  
 404 region has the spherical shape). The Fourier series elements in the parentheses  
 405 in Eq. 1.3 represent different kinds of flow. The first value: "1" represents the  
 406 *radial flow* - an isotropic flow in every direction. Next coefficient  $v_1$  is responsible  
 407 for *direct flow*. The  $v_2$  coefficient is a measure of elliptic anisotropy (*elliptic flow*).  
 408 The  $v_2$  has to build up in the early stage of a collision - later the system becomes  
 409 too dilute: space asymmetry and the pressure gradient vanish. Therefore the  
 410 observation of elliptic flow means that the created matter was in fact a strongly  
 411 interacting matter.

412 The  $v_2$  coefficient was measured already at CERN SPS, LHC and RHIC. For  
 413 the first time hydrodynamics successfully described the collision dynamics as the

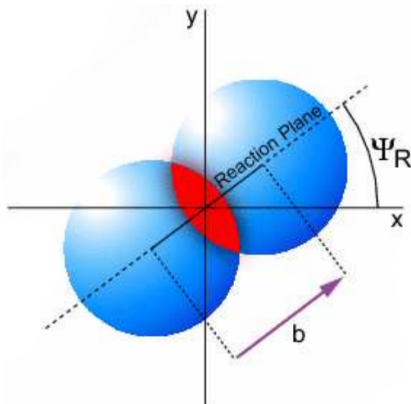


Figure 1.9: Cross-section of a heavy ion collision in a transverse plane. The  $b$  parameter is an *impact parameter* - a distance between centers of nuclei during a collision. An impact parameter is related with the centrality of a collision and a volume of the quark-gluon plasma [12].

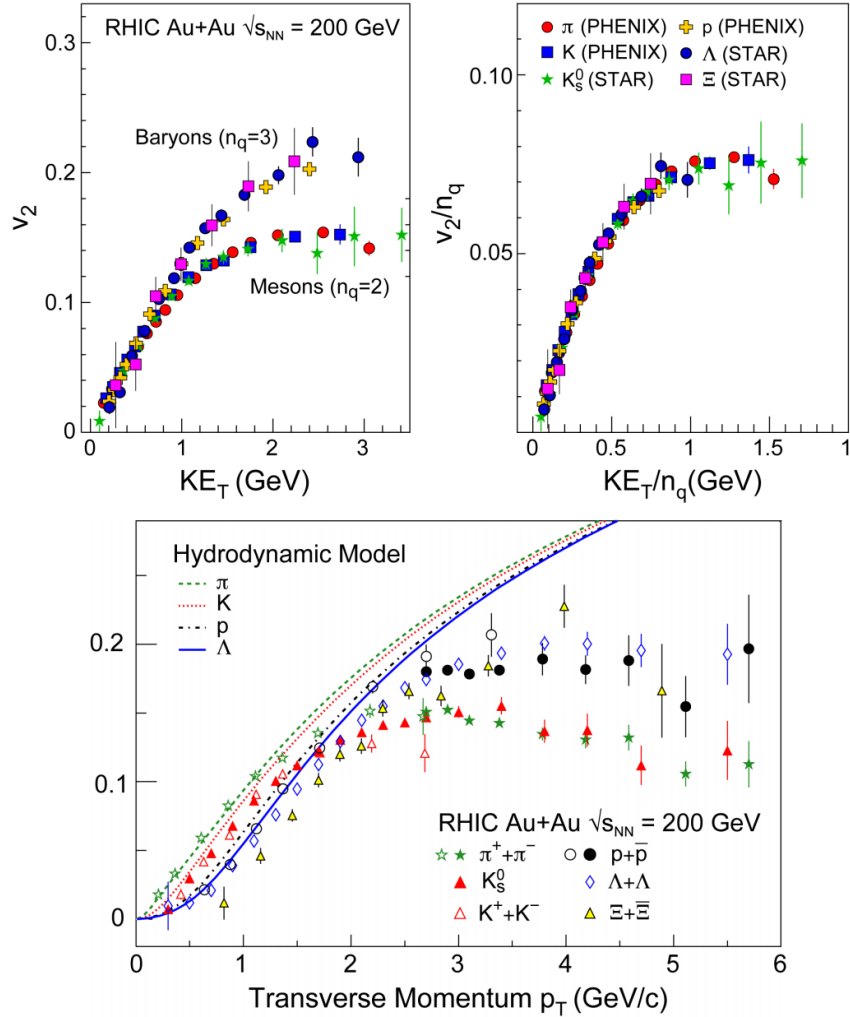


Figure 1.10: *Lower:* The elliptic flow  $v_2$  follows the hydrodynamical predictions for an ideal fluid perfectly. Note that > 99% of all final hadrons have  $p_T < 1.5 \text{ GeV}/c$ . *Upper left:* The  $v_2$  plotted versus transverse kinetic energy  $KE_T = m_T - m_0 = \sqrt{p_T^2 + m_0^2} - m_0$ . The  $v_2$  follows different universal curves for mesons and baryons. *Upper right:* When scaled by the number of valence quarks, the  $v_2$  follows the same universal curve for all hadrons and for all values of scaled transverse kinetic energy [13].

414 measured  $v_2$  reached hydrodynamic limit (Fig. 1.10). As expected, there is a mass  
 415 ordering of  $v_2$  as a function of  $p_T$  (lower plot in the Fig. 1.10) with pions having  
 416 the largest and protons the smallest anisotropy. In the upper plots in the Fig. 1.10  
 417 there is a  $v_2$  as a function of transverse kinetic energy. The left plot shows two  
 418 universal trend lines for baryons and mesons. After the scaling of  $v_2$  and the

419 kinetic energy by the number of valence quarks, all of the hadrons follow the  
 420 same universal curve. Those plots show that strong collectivity is observed in  
 421 heavy ion collisions.

422 **Transverse radial flow**

423 Elliptic flow described previously is caused by the pressure gradients which  
 424 must also produce a more simple collective behaviour of matter - a movement  
 425 inside-out, called radial flow. Particles are pushed to higher momenta and they  
 426 move away from the center of the collision. A source not showing collective  
 427 behaviour, like pp collisions, produces particle spectra that can be fitted by a  
 428 power-law [8]:

$$\frac{1}{2\pi p_T} \frac{d^2 N}{dp_T d\eta} = C \left( 1 + \frac{p_T}{p_0} \right)^{-n} . \quad (1.5)$$

429 The  $\eta$  variable is *pseudorapidity* defined as follows:

$$\eta = \frac{1}{2} \ln \left( \frac{p + p_L}{p - p_L} \right) = -\ln \left( \frac{\theta}{2} \right) , \quad (1.6)$$

where  $\theta$  is an emission angle  $\cos \theta = p_L/p$ .

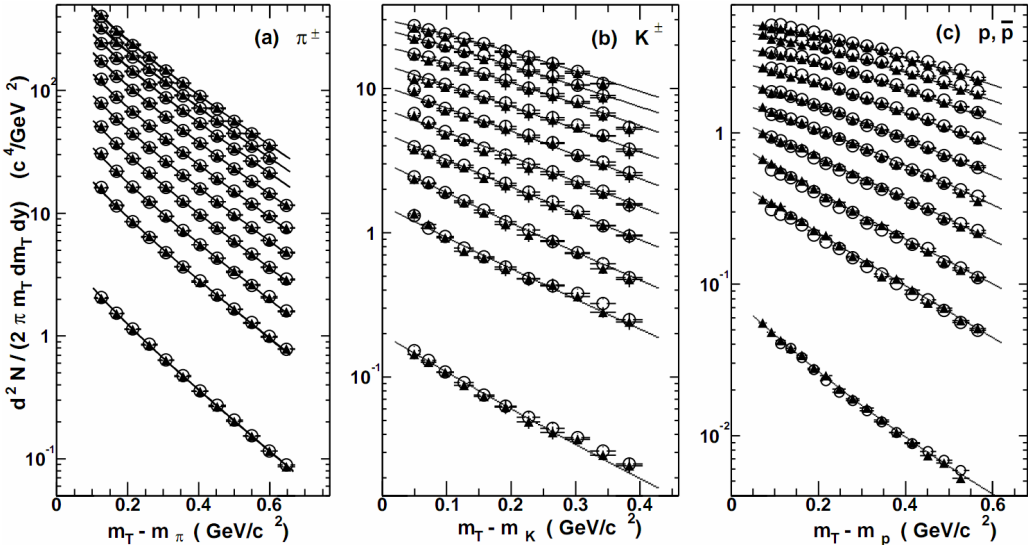


Figure 1.11: Invariant yield of particles versus transverse mass  $m_T = \sqrt{p_T^2 + m_0^2}$  for  $\pi^\pm$ ,  $K^\pm$ ,  $p$  and  $\bar{p}$  at mid-rapidity for p+p collisions (bottom) and Au+Au events from 70-80% (second bottom) to 0-5% (top) centrality [14].

430  
 431 The hydrodynamical expansion of a system gives the same flow velocity kick  
 432 for different kinds of particles - ones with bigger masses will gain larger  $p_T$  boost.  
 433 This causes increase of the yield of particles with larger transverse momenta. In

the invariant yield plots one can observe the decrease of the slope parameter, especially for the heavier hadrons. This is presented in the Fig. 1.11. The most affected spectra are ones of kaons (b) and protons (c). One can notice decrease of the slope parameter for heavy ion collisions (plots from second bottom to top) comparing to the proton-proton collisions (bottom ones), where no boost from radial flow should occur [8].

Another signature of a transverse radial flow is a dependence of HBT radii on a pair transverse momentum. Detailed description of this effect is presented in the Section 3.4.

#### 443 Direct photons

444 The direct photons are photons, which are not coming from the final state  
445 hadrons decays. Their sources can be various interaction from charged particles  
446 created in the collision, either at the partonic or at the hadronic level. Direct  
447 photons are considered to be an excellent probe of the early stage of the collision.  
448 This is because their mean free path is very large when compared to the size of  
449 created system in the collision. Thus photons created at the early stage leave the  
450 system without suffering any interaction and retain information about this stage,  
451 in particular about its temperature.

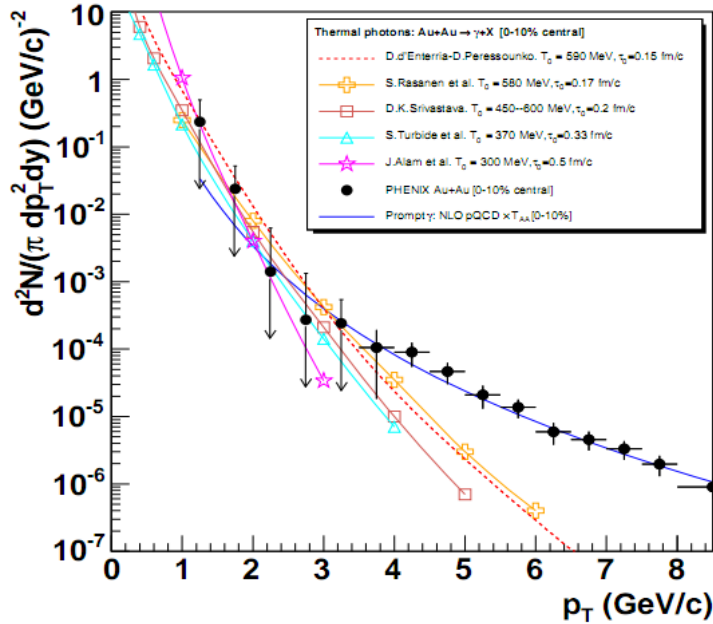


Figure 1.12: Thermal photons spectra for the central Au+Au collisions at  $\sqrt{s_{NN}} = 200$  GeV computed within different hydrodynamical models compared with the pQCD calculations (solid line) and experimental data from PHENIX (black dots) [15].

One can distinguish two kinds of direct photons: *thermal* and *prompt*. Thermal photons can be emitted from the strong processes in the quark-gluon plasma involving quarks and gluons or hot hadronic matter (e.g. processes:  $\pi\pi \rightarrow \rho\gamma$ ,  $\pi\rho \rightarrow \pi\gamma$ ). Thermal photons can be observed in the low  $p_T$  region. Prompt photons are believed to come from “hard” collisions of initial state partons belonging to the colliding nuclei. The prompt photons can be described using the pQCD. They will dominate the high  $p_T$  region. The analysis of transverse momentum of spectra of direct photons revealed, that the temperature of the source of thermal photons produced in heavy ion collisions at RHIC is in the range 300–600 MeV (Fig. 1.12). Hence the direct photons had to come from a system whose temperature is far above from the critical temperature for QGP creation.

### Puzzle in di-lepton mass spectrum

The invariant mass spectra (Fig. 1.13) of lepton pairs reveal many peaks corresponding to direct decays of various mesons into a lepton pair. The continuous background in this plot is caused by the decays of hadrons into more than two leptons (including so-called *Dalitz decays* into a lepton pair and a photon). Particular hadron decay channels, which contribute to this spectrum are shown

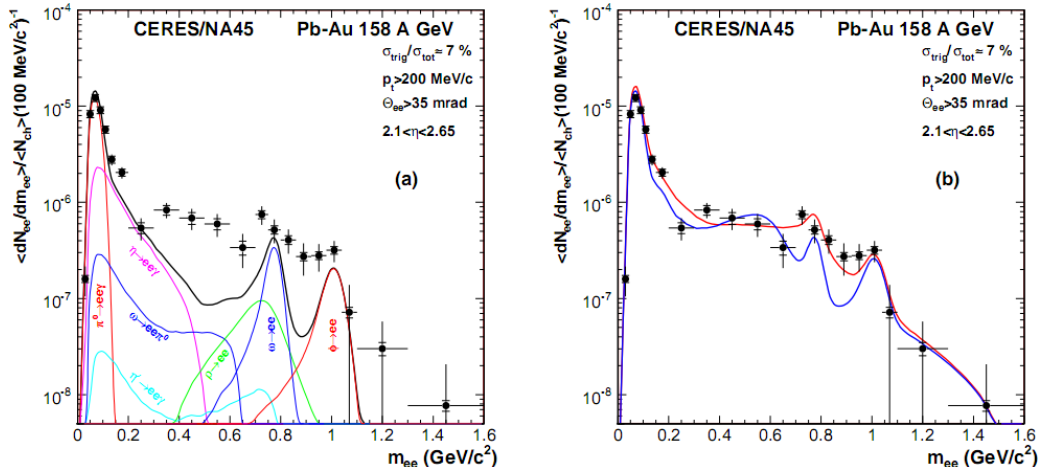


Figure 1.13: Left: Invariant mass spectrum of  $e^+ - e^-$  pairs in Pb+Au collisions at 158A GeV compared to the sum coming from the hadron decays predictions. Right: The expectations coming from model calculations assuming a dropping of the  $\rho$  mass (blue) or a spread of the  $\rho$  width in the medium (red) [16].

in Fig. 1.13 with the coloured lines and their sum with the black one. The sum (called *the hadronic cocktail*) of various components describes experimental spectra coming from the simple collisions (like p+p or p+A) quite well with the statistical and systematical uncertainties [9]. This situation is different considering more complicated systems i.e. A+A. Spectra coming from Pb+Au collisions are presented on the plots in the Fig. 1.13. The “hadronic cocktail” does not describe

the data, in the mass range between the  $\pi$  and the  $\rho$  mesons a significant excess of electron pairs over the calculated sum is observed. Theoretical explanation of this phenomenon assumes modification of the spectral shape of vector mesons in a dense medium. Two different interpretations of this increase were proposed: a decrease of meson mass with the medium density and increase of the meson width in the dense medium. In principle, one could think of simultaneous occurrence of both effects: mass shift and resonance broadening. Experimental results coming from the CERES disfavour the mass shift hypothesis indicating only broadening of resonance peaks (Fig. 1.13b) [9].

#### 484 Jet quenching

A jet is defined as a group of particles with close vector momenta and high energies. It has its beginning when the two partons are going in opposite directions and have energy big enough to produce new quark-antiquark pair and then radiate gluons. This process can be repeated many times and it results in two back-to-back jets of hadrons. It has been found that jets in the opposite hemisphere (*away-side jets*) show a very different pattern in d+Au and Au+Au collisions. This is shown in the azimuthal correlations in the Fig. 1.14. In d+Au collisions, like in p+p, a pronounced away-side jet appears around  $\Delta\phi = \pi$ , exactly opposite to the trigger jet, which is typical for di-jet events. In central Au+Au collisions the away-side jet is suppressed. When the jet has its beginning near the surface of the quark-gluon plasma, one of the jets (*near-side jet*) leaves the system almost without any interactions. This jet is visible on the correlation plot as a high peak

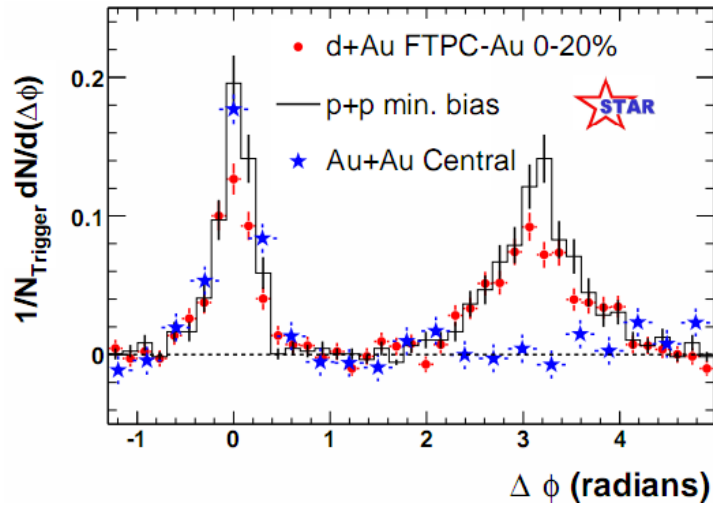


Figure 1.14: Azimuthal angle difference  $\Delta\phi$  distributions for different colliding systems at  $\sqrt{s_{NN}} = 200$  GeV. Transverse momentum cut:  $p_T > 2$  GeV. For the Au+Au collisions the away-side jet is missing [17].

497 at  $\Delta\phi = 0$ . However, the jet moving towards the opposite direction has to penetrate  
498 a dense medium. The interaction with the plasma causes energy dissipation  
499 of particles and is visible on an azimuthal correlation plot as a disappearance of  
500 the away-side jet [9].

501 **Chapter 2**

502 **Therminator model**

503     THERMINATOR [18] is a Monte Carlo event generator designed to investigate  
504     the particle production in the relativistic heavy ion collisions. The functionality  
505     of the code includes a generation of the stable particles and unstable resonances  
506     at the chosen hypersurface model. It performs the statistical hadronization which  
507     is followed by space-time evolution of particles and the decay of resonances. The  
508     key element of this method is an inclusion of a complete list of hadronic reso-  
509     nances, which contribute very significantly to the observables. The second version  
510     of THERMINATOR [19] comes with a possibility to incorporate any shape of freeze-  
511     out hypersurface and the expansion velocity field, especially those generated ex-  
512     ternally with various hydrodynamic codes. The event generator is written in C++  
513     programming language and it employs ROOT [20] analysis framework.

514 **2.1 (3+1)-dimensional viscous hydrodynamics**

515     Most of the relativistic viscous hydrodynamic calculations are done in  
516     (2+1)-dimensions. Such simplification assumes boost-invariance of a matter  
517     created in a collision. Experimental data reveals that no boost-invariant region is  
518     formed in the collisions [21]. Hence, for the better description of created system  
519     a (3+1)-dimensional model is required.

520     In the four dimensional relativistic dynamics one can describe a system  
521     using a space-time four-vector  $x^\nu = (ct, x, y, z)$ , a velocity four-vector  
522      $u^\nu = \gamma(c, v_x, v_y, v_z)$  and a energy-momentum tensor  $T^{\mu\nu}$ . The particular  
523     components of  $T^{\mu\nu}$  have a following meaning:

- 524       •  $T^{00}$  - an energy density,
- 525       •  $cT^{0\alpha}$  - an energy flux across a surface  $x^\alpha$ ,
- 526       •  $T^{\alpha 0}$  - an  $\alpha$ -momentum flux across a surface  $x^\alpha$  multiplied by  $c$ ,
- 527       •  $T^{\alpha\beta}$  - components of momentum flux density tensor,

528 where  $\gamma = (1 - v^2/c^2)^{-1/2}$  is Lorentz factor and  $\alpha, \beta \in \{1, 2, 3\}$ . Using  $u^\nu$  one can  
 529 express  $T^{\mu\nu}$  as follows [22]:

$$T_0^{\mu\nu} = (e + p)u^\mu u^\nu - pg^{\mu\nu} \quad (2.1)$$

530 where  $e$  is an energy density,  $p$  is a pressure and  $g^{\mu\nu}$  is an inverse metric tensor:

$$g^{\mu\nu} = \begin{bmatrix} 1 & 0 & 0 & 0 \\ 0 & -1 & 0 & 0 \\ 0 & 0 & -1 & 0 \\ 0 & 0 & 0 & -1 \end{bmatrix}. \quad (2.2)$$

531 The presented version of energy-momentum tensor (Eq. 2.1) can be used to de-  
 532 scribe dynamics of a perfect fluid. To take into account influence of viscosity,  
 533 one has to apply the following corrections coming from shear  $\pi^{\mu\nu}$  and bulk  $\Pi$   
 534 viscosities [23]:

$$T^{\mu\nu} = T_0^{\mu\nu} + \pi^{\mu\nu} + \Pi(g^{\mu\nu} - u^\mu u^\nu). \quad (2.3)$$

535 The stress tensor  $\pi^{\mu\nu}$  and the bulk viscosity  $\Pi$  are solutions of dynamical equa-  
 536 tions in the second order viscous hydrodynamic framework [22]. The compari-  
 537 son of hydrodynamics calculations with the experimental results reveal, that the  
 538 shear viscosity divided by entropy  $\eta/s$  has to be small and close to the AdS/CFT  
 539 estimate  $\eta/s = 0.08$  [23, 24]. The bulk viscosity over entropy value used in calcu-  
 540 lations is  $\zeta/s = 0.04$  [23].

541 When using  $T^{\mu\nu}$  to describe system evolving close to local thermodynamic  
 542 equilibrium, relativistic hydrodynamic equations in a form of:

$$\partial_\mu T^{\mu\nu} = 0 \quad (2.4)$$

543 can be used to describe the dynamics of the local energy density, pressure and  
 544 flow velocity.

545 Hydrodynamic calculations are starting from the Glauber<sup>1</sup> model initial con-  
 546 ditions. The collective expansion of a fluid ends at the freeze-out hypersurface.  
 547 That surface is usually defined as a constant temperature surface, or equivalently  
 548 as a cut-off in local energy density. The freeze-out is assumed to occur at the  
 549 temperature  $T = 140$  MeV.

## 550 2.2 Statistical hadronization

551 Statistical description of heavy ion collision has been successfully used to  
 552 quantitatively describe the *soft* physics, i.e. the regime with the transverse mo-  
 553 mentum not exceeding 2 GeV. The basic assumption of the statistical approach of  
 554 evolution of the quark-gluon plasma is that at some point of the space-time evol-  
 555 ution of the fireball, the thermal equilibrium is reached. When the system is in the

---

<sup>1</sup>The Glauber Model is used to calculate “geometrical” parameters of a collision like an impact parameter, number of participating nucleons or number of binary collisions.

556 thermal equilibrium the local phase-space densities of particles follow the Fermi-  
 557 Dirac or Bose-Einstein statistical distributions. At the end of the plasma expan-  
 558 sion, the freeze-out occurs. The freeze-out model incorporated in THERMINATOR  
 559 assumes, that chemical and thermal freeze-outs occur at the same time.

560 **2.2.1 Cooper-Frye formalism**

561 The result of the hydrodynamic calculations is the freeze-out hyper-  
 562 surface  $\Sigma^\mu$ . A three-dimensional element of the surface is defined as [19]

$$563 \quad d\Sigma_\mu = \epsilon_{\mu\alpha\beta\gamma} \frac{\partial x^\alpha}{\partial \alpha} \frac{\partial x^\beta}{\partial \beta} \frac{\partial x^\gamma}{\partial \gamma} d\alpha d\beta d\gamma, \quad (2.5)$$

564 where  $\epsilon_{\mu\alpha\beta\gamma}$  is the Levi-Civita tensor and the variables  $\alpha, \beta, \gamma \in \{1, 2, 3\}$  are used  
 565 to parametrize the three-dimensional freeze-out hypersurface in the Minkowski  
 566 four-dimensional space. The Levi-Civita tensor is equal to 1 when the indices  
 567 form an even permutation (eg.  $\epsilon_{0123}$ ), to -1 when the permutation is odd (e.g.  
 568  $\epsilon_{2134}$ ) and has a value of 0 if any index is repeated. Therefore [19],

$$569 \quad d\Sigma_0 = \begin{vmatrix} \frac{\partial x}{\partial \alpha} & \frac{\partial x}{\partial \beta} & \frac{\partial x}{\partial \gamma} \\ \frac{\partial y}{\partial \alpha} & \frac{\partial y}{\partial \beta} & \frac{\partial y}{\partial \gamma} \\ \frac{\partial z}{\partial \alpha} & \frac{\partial z}{\partial \beta} & \frac{\partial z}{\partial \gamma} \end{vmatrix} d\alpha d\beta d\gamma \quad (2.6)$$

570 and the remaining components are obtained by cyclic permutations of  $t, x, y$   
 571 and  $z$ .

One can obtain the number of hadrons produced on the hypersurface  $\Sigma^\mu$  from  
 the Cooper-Frye formalism. The following integral yields the total number of  
 created particles [19]:

$$572 \quad N = (2s + 1) \int \frac{d^3 p}{(2\pi)^3 E_p} \int d\Sigma_\mu p^\mu f(p_\mu u^\mu), \quad (2.7)$$

573 where  $f(p_\mu u^\mu)$  is the phase-space distribution of particles (for stable ones and res-  
 574 onances). One can simply derive from Eq. 2.7, the dependence of the momentum  
 575 density [25]:

$$E \frac{d^3 N}{dp^3} = \int d\Sigma_\mu f(p_\mu u^\mu) p^\mu. \quad (2.8)$$

574 The momentum distribution  $f$  contains non-equilibrium corrections:

$$f = f_0 + \delta f_{shear} + \delta f_{bulk}, \quad (2.9)$$

575 where

$$f_0(p_\mu u^\mu) = \left\{ \exp \left[ \frac{p_\mu u^\mu - (B\mu_B + I_3\mu_{I_3} + S\mu_S + C\mu_C)}{T} \right] \pm 1 \right\}^{-1}. \quad (2.10)$$

576 In case of fermions, in the Eq. 2.10 there is a plus sign and for bosons, minus  
 577 sign respectively. The thermodynamic quantities appearing in the  $f_0(\cdot)$  are  $T$  -  
 578 temperature,  $\mu_B$  - baryon chemical potential,  $\mu_{I_3}$  - isospin chemical potential,  $\mu_S$   
 579 - strange chemical potential,  $\mu_C$  - charmed chemical potential and the  $s$  is a spin of  
 580 a particle. The hydrodynamic calculations yield the flow velocity at freeze-out as  
 581 well as the stress and bulk viscosity tensors required to calculate non-equilibrium  
 582 corrections to the momentum distribution used in Eq. 2.7. The term coming from  
 583 shear viscosity has a form [23]

$$\delta f_{shear} = f_0(1 \pm f_0) \frac{1}{2T^2(e + p)} p^\mu p^\nu \pi_{\mu\nu} \quad (2.11)$$

584 and bulk viscosity

$$\delta f_{bulk} = C f_0(1 \pm f_0) \left( \frac{(u^\mu p_\mu)^2}{3u^\mu p_\mu} - c_s^2 u^\mu p_\mu \right) \Pi \quad (2.12)$$

585 where  $c_s$  is sound velocity and

$$\frac{1}{C} = \frac{1}{3} \frac{1}{(2\pi)^3} \sum_{hadrons} \int d^3 p \frac{m^2}{E} f_0(1 \pm f_0) \left( \frac{p^2}{3E} - c_s^2 E \right). \quad (2.13)$$

### 586 2.3 Events generation procedure

587 The equations presented in the previous section are directly used in the  
 588 THERMINATOR to generate the primordial hadrons (created during freeze-out)  
 589 with the Monte-Carlo method. This procedure consists of 3 main steps, where  
 590 the first two are performed only once per given parameter set. After the  
 591 generation of primordial particles, the cascade decay of unstable resonances is  
 592 performed.

#### 593 Determination of a maximum of an integrand

594 In order to generate particles through a Monte Carlo method, the maximum  
 595 value of the distribution in the right-hand-side of Eq. 2.7 must be known. To find  
 596 this number, THERMINATOR performs a generation of a sample consisting of a  
 597 large number of particles. For each particle the value of a distribution is cal-  
 598 culated and the maximum value  $f_{max}$  of the sample is stored. A large enough  
 599 sample of particles guarantees that  $f_{max}$  found in this procedure is a good es-  
 600 timate of the maximum value of a distribution in Eq. 2.7. This maximum value  
 601 depends on a particle type and values of parameters, but does not change from  
 602 event to event, hence this procedure is performed once, at the beginning of the  
 603 events generation [18].

604 **Multiplicity calculation**

605 In order to generate events, a multiplicity of each particle must be known.  
 606 The multiplicities are obtained through a numerical integration of distribution  
 607 functions (Eq. 2.7) in the given integration ranges determined by the model para-  
 608 meters. The multiplicities also depend only on the model parameters and they  
 609 are also only calculated once at the beginning of the event generation [18].

610 **Events and particles generation**

611 Each of the events produced by THERMINATOR are generated separately. At  
 612 first, the multiplicities for each of particle type are generated as random numbers  
 613 from a Poisson distribution, with the mean being the average particle multipli-  
 614 city determined in the previous step. Then the program proceeds to generate  
 615 particles from the heaviest to the lightest particle type. In essence, this procedure  
 616 is a generation of the set of six random numbers: three components of particle's  
 617 momentum ( $p_x, p_y, p_z$ ) and three parameters providing space-time coordinates  
 618 on a freeze-out hypersurface ( $\zeta, \phi_s, \theta$ ). Event generation procedure is based on  
 619 von Neumann's acceptance-rejection algorithm. Firstly, the integrand in Eq. 2.7  
 620 is calculated using given set of numbers. Subsequently, a random number from  
 621 uniform distribution over  $[0; f_{max}]$  is compared to the value of integrand. If it  
 622 is lower, then the set of numbers is stored as actual particle. If this condition  
 623 was not satisfied, a new set is generated. This procedure is repeated until the  
 624 determined number of particles of each kind is generated. At this point all prim-  
 625 ordial particles (stable and resonances) have been generated and stored in the  
 626 event [18].

627 **Decays of unstable particles**

628 In the next step of event generation, a simulation of decays of unstable res-  
 629 onances is performed. A particle is considered as unstable when it has non-zero  
 630 width  $\Gamma$  defined in the input files of THERMINATOR. The decays proceed sequen-  
 631 tially from the heaviest particles to the lightest. Unstable products of decays are  
 632 added to the particles generated in the current event and are processed in the  
 633 subsequent steps. If a particle has several decay channels, one of them is selec-  
 634 ted randomly with the appropriate probability corresponding to the branching  
 635 ratio provided in the input files. THERMINATOR in the hadronic cascade process  
 636 performs two-body and three-body decays.

637 At the beginning of the cascade decay, the lifetime  $\tau$  of a particle with mass  
 638  $M$ , moving with the four-momentum  $p^\mu$ , is generated randomly according to the  
 639 exponential decay law  $\exp(-\Gamma\tau)$ . When the lifetime is known, the point of its  
 640 decay is calculated as [18]:

$$x_{decay}^\mu = x_{origin}^\mu + \frac{p^\mu}{M}\tau, \quad (2.14)$$

641 where  $x_{\text{origin}}^\mu$  is a space-time position, where the unstable particle was generated.  
 642 At the  $x_{\text{decay}}^\mu$  point decay occurs and daughter particles with energies and mo-  
 643 ments determined by the conservation laws are generated. Fig. 2.1 illustrates the  
 cascade decay process [18].

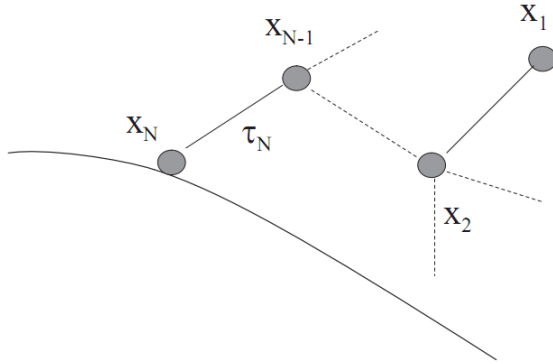


Figure 2.1: The cascade decay in the single freeze-out model. An unstable resonance  $x_N$  is formed at the freeze-out hypersurface and travels for the time  $\tau_N$  depending on its lifetime and decays. If the products are also resonances ( $x_{N-1}$ ,  $x_2$ ) they decay further until the stable particles are formed ( $x_1$ ) [18].

645 **Chapter 3**

646 **Particle interferometry**

647 Two-particle interferometry (also called *femtoscopy*) gives a possibility to  
648 investigate space-time characteristics of the particle-emitting source created  
649 in heavy ion collisions. Through the study of particle correlations, their  
650 momentum distributions can be used to obtain information about the spatial  
651 extent of the created system. Using this method, one can measure sizes of the  
652 order of  $10^{-15}$  m and time of the order of  $10^{-23}$  s.

653 **3.1 HBT interferometry**

654 In the 1956 Robert Hanbury Brown and Richard Q. Twiss proposed a method  
655 which allowed to investigate angular dimensions of stars through analysis of  
656 interference between photons. They performed a measurement of the intensity  
657 of a beam of light coming from a star using two separated detectors. In a sig-  
658 nal plotted as a function of distance between detectors an interference effect was  
659 observed, revealing a positive correlation, despite the fact that no phase inform-  
660 ation was collected. Hanbury, Brown and Twiss used this interference signal to  
661 calculate the angular size of a star with the excellent resolution. This method was  
662 designed to be used in astronomy, however HBT interferometry can be used also  
663 to measure extent of any emitting source. Therefore it was adapted to heavy ion  
664 collisions to investigate dimensions of a particle-emitting source [8].

665 **3.2 Theoretical approach**

666 Intensity interferometry in heavy ion physics uses similar mathematical form-  
667 alism as the astronomy HBT measurement. The difference between them is that  
668 femtoscopy uses a two-particle relative momentum and yields the space-time  
669 picture of a source, whereas the latter method uses the distance between detect-  
670 ors to calculate angular size of the star.

671 **3.2.1 Conventions used**

672 In heavy ion collisions to describe particular directions, components of mo-  
 673 mentum and location of particles, one uses naming convention called the Bertsch-  
 Pratt coordinate system. This system is presented in the Fig. 3.1. The three dir-

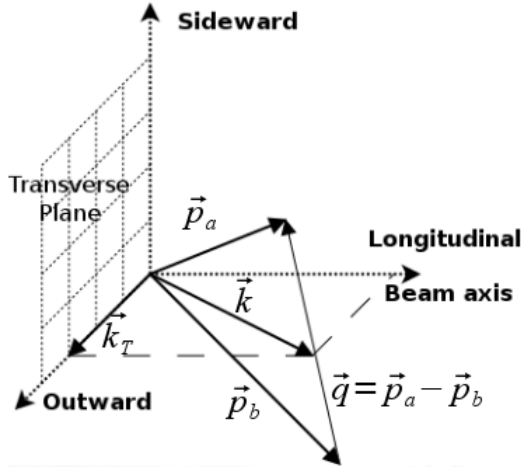


Figure 3.1: Bertsch-Pratt direction naming convention used in heavy ion collision.

674  
 675 ections are called *longitudinal*, *outward* and *sideward*. The longitudinal direction  
 676 is parallel to the beam axis. The plane perpendicular to the beam axis is called  
 677 a *transverse plane*. A projection of a particle pair momentum  $\mathbf{k} = (\mathbf{p}_a + \mathbf{p}_b)/2$   
 678 on a transverse plane (a *transverse momentum*  $\mathbf{k}_T$ ) determines *outward* direction:  
 679  $(\mathbf{k})_{out} = \mathbf{k}_T$ . A direction perpendicular to the longitudinal and outward is called  
 680 *sideward*.

681 A particle pair is usually described using two coordinate systems. The first  
 682 one, *Longitudinally Co-Moving System* (LCMS) is moving along the particle pair  
 683 with the longitudinal direction, in other words, the pair longitudinal momentum  
 684 vanishes:  $(\mathbf{p}_a)_{long} = -(\mathbf{p}_b)_{long}$ . The second system is called *Pair Rest Frame* (PRF).  
 685 In the PRF the centre of mass rests:  $\mathbf{p}_a = -\mathbf{p}_b$ . Variables which are expressed in  
 686 the PRF are marked with a star (e.g.  $\mathbf{k}^*$ ).

The transition of space-time coordinates from LCMS to PRF is simply  
 a boost along the outward direction, with the transverse velocity of the  
 pair  $\beta_T = (\mathbf{v}/c)_{out}$  [26]:

$$r_{out}^* = \gamma_T(r_{out} - \beta_T \Delta t) \quad (3.1)$$

$$r_{side}^* = r_{side} \quad (3.2)$$

$$r_{long}^* = r_{long} \quad (3.3)$$

$$\Delta t^* = \gamma_T(\Delta t - \beta_T r_{out}), \quad (3.4)$$

687 where  $\gamma_T = (1 - \beta_T^2)^{-1/2}$  is the Lorentz factor. However, in calculations performed

in this work the equal time approximation is used, which assumes that particles in a pair were produced at the same time in PRF - the  $\Delta t^*$  is neglected.

The most important variables used to describe particle pair are their total momentum  $\mathbf{P} = \mathbf{p}_a + \mathbf{p}_b$  and relative momentum  $\mathbf{q} = \mathbf{p}_a - \mathbf{p}_b$ . In the PRF one has  $\mathbf{q} = 2\mathbf{k}^*$ , where  $\mathbf{k}^*$  is a momentum of the first particle in PRF.

### 3.2.2 Two particle wave function

Let us consider two identical particles with momenta  $\mathbf{p}_1$  and  $\mathbf{p}_2$  emitted from space points  $\mathbf{x}_1$  and  $\mathbf{x}_2$ . Those emitted particles can be treated as two incoherent waves. If the particles are identical, they are also indistinguishable, therefore one

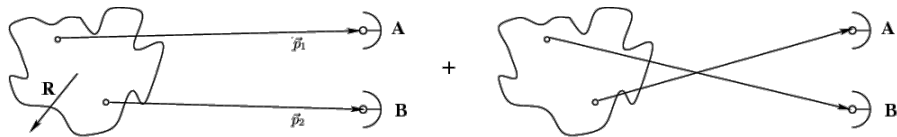


Figure 3.2: The pair wave function is a superposition of all possible states. In case of particle interferometry it includes two cases: particles with momenta  $p_1, p_2$  registered by detectors A, B and  $p_1, p_2$  registered by B, A respectively.

has also take into account the scenario, where the particle with momentum  $\mathbf{p}_1$  is emitted from  $\mathbf{x}_2$  and particle  $\mathbf{p}_2$  from  $\mathbf{x}_1$  (Fig. 3.2). In such case, the wave function describing behaviour of a pair has to contain both components [8]:

$$\Psi_{ab}(\mathbf{q}) = \frac{1}{\sqrt{2}} [\exp(-i\mathbf{p}_1\mathbf{x}_1 - i\mathbf{p}_2\mathbf{x}_2) \pm \exp(-i\mathbf{p}_2\mathbf{x}_1 - i\mathbf{p}_1\mathbf{x}_2)] . \quad (3.5)$$

A two particle wave function of identical bosons is symmetric ("+" sign in Eq. 3.5) and in case of identical fermions - antisymmetric ("-" sign). This anti-symmetrization or symmetrization implies the correlation effect coming from the Fermi-Dirac or Bose-Einstein statistics accordingly.

To provide full description of a system consisting of two charged hadrons, one has to include in the wave function besides quantum statistics also Coulomb and strong Final State Interactions. The aim of this work is an analysis of femtoscopic radii proportional to the inverse of a width of a correlation function (for detailed description see Section 3.2.4). Since we are not interested in the direct comparison of experimental correlation functions with their analytical forms, the following simplification can be made. A width of identical particles correlation function is determined by effects coming from quantum statistics, hence one can ignore influence of Final State Interactions, which in this case is small. Taking into account only quantum statistics can reduce complexity of calculations and save computation time.

715 **3.2.3 Source emission function**

716 To describe particle emitting source, one uses a single emission function [26]:

717

$$S_A(\mathbf{x}_1, \mathbf{p}_1) = \int S(\mathbf{x}_1, \mathbf{p}_1, \mathbf{x}_2, \mathbf{p}_2, \dots, \mathbf{x}_N, \mathbf{p}_N) d\mathbf{x}_2 d\mathbf{p}_2 \dots d\mathbf{x}_N d\mathbf{p}_N \quad (3.6)$$

718 and a two-particle one:

$$S_{AB}(\mathbf{x}_1, \mathbf{p}_1, \mathbf{x}_2, \mathbf{p}_2) = \int S(\mathbf{x}_1, \mathbf{p}_1, \mathbf{x}_2, \mathbf{p}_2, \dots, \mathbf{x}_N, \mathbf{p}_N) d\mathbf{x}_3 d\mathbf{p}_3 \dots d\mathbf{x}_N d\mathbf{p}_N . \quad (3.7)$$

719 Emission function  $S(\cdot)$  can be interpreted as a probability to emit a particle, or  
 720 a pair of particles from a given space-time point with a given momentum. In  
 721 principle, the source emission function should encode all physics aspects of the  
 722 particle emission process i.e. the symmetrization for bosons and fermions, as  
 723 well as the two-body and many body Final State Interactions. Instead of this,  
 724 one assume that each particle's emission process is independent - the interac-  
 725 tion between final-state particles after their creation is independent from their  
 726 emission process. The assumption of this independence allows to construct two-  
 727 particle emission function from single particle emission functions via a convolu-  
 728 tion [26]:

$$S(\mathbf{k}^*, \mathbf{r}^*) = \int S_A(\mathbf{p}_1, \mathbf{x}_1) S_B(\mathbf{p}_2, \mathbf{x}_2) \delta \left[ \mathbf{k}^* - \frac{\mathbf{p}_1 + \mathbf{p}_2}{2} \right] \delta [\mathbf{r}^* - (\mathbf{x}_1 + \mathbf{x}_2)] \times d^4 \mathbf{x}_1 d^4 \mathbf{x}_2 d^4 \mathbf{x}_1 d^3 \mathbf{p}_1 d^3 \mathbf{p}_2 \quad (3.8)$$

729 In case of identical particles, ( $S_A = S_B$ ) several simplifications can be made. A  
 730 convolution of the two identical Gaussian distributions is also a Gaussian distri-  
 731 bution with  $\sigma$  multiplied by  $\sqrt{2}$ . Femtoscopy can give information only about  
 732 two-particle emission function, but when considering Gaussian distribution as  
 733 a source function in Eq. 3.8, one can obtain a  $\sigma$  of a single emission function  
 734 from a two-particle emission function. The Eq. 3.8 is not reversible - an inform-  
 735 ation about  $S_A(\cdot)$  cannot be derived from  $S_{AB}(\cdot)$ . An exception from this rule  
 736 is a Gaussian source function, hence it is often used in femtoscopic calculations.  
 737 Considering pairs of identical particles, an emission function is assumed to be  
 738 described by the following equation in the Pair Rest Frame [26]:

$$S_{1D}^{PRF}(\mathbf{r}^*) = \exp \left( -\frac{r_{out}^{*2} + r_{side}^{*2} + r_{long}^{*2}}{4R_{inv}^2} \right) . \quad (3.9)$$

To change from the three-dimensional variables to the one-dimensional variable  
 one requires introduction of the proper Jacobian  $r^{*2}$ .

$$S_{1D}^{PRF}(r^*) = r^{*2} \exp \left( -\frac{r^{*2}}{4R_{inv}^2} \right) . \quad (3.10)$$

739 The “4” in the denominator before the “standard deviation”  $R_{inv}$  in the Gaussian  
 740 distribution comes from the convolution of the two Gaussian distributions,  
 741 which multiplies the  $R_{inv}$  by a factor of  $\sqrt{2}$ .

A more complex form of emission function was used by all RHIC and SPS experiments in identical pion femtoscopy:

$$S_{3D}^{LCMS}(\mathbf{r}) = \exp \left( -\frac{r_{out}^2}{4R_{out}^2} - \frac{r_{side}^2}{4R_{side}^2} - \frac{r_{long}^2}{4R_{long}^2} \right). \quad (3.11)$$

742 The main difference of this source function is that it has three different and inde-  
 743 pendent widths  $R_{out}$ ,  $R_{side}$ ,  $R_{long}$  and they are defined in the LCMS, not in PRF.  
 744 Unlike in PRF, in LCMS an equal-time approximation is not used. For identical  
 745 particles this is not a problem - only Coulomb interaction inside a wave function  
 746 depends on  $\Delta t$ .

#### 747 Relationship between one-dimensional and three-dimensional source sizes

748 Up to now, most of femtoscopic measurements were limited only to averaged  
 749 source size  $R_{av}^L$  (the letter “L” in superscript stands for LCMS):

$$S_{1D}^{LCMS}(\mathbf{r}) = \exp \left( -\frac{r_{out}^2 + r_{side}^2 + r_{long}^2}{2R_{av}^L} \right). \quad (3.12)$$

750 The relationship between between  $S_{1D}^{LCMS}(\cdot)$  and  $S_{3D}^{LCMS}(\cdot)$  is given by:

$$S_{3D}^{LCMS}(r) = \int \exp \left( -\frac{r_{out}^2}{2R_{out}^L} - \frac{r_{side}^2}{2R_{side}^L} - \frac{r_{long}^2}{2R_{long}^L} \right) \times \delta \left( r - \sqrt{r_{out}^2 + r_{side}^2 + r_{long}^2} \right) dr_{out} dr_{side} dr_{long}. \quad (3.13)$$

751 The one-dimensional source size corresponding to the three-dimensional one can  
 752 be approximated by the following form:

$$S_{1D}^{LCMS}(r) = r^2 \exp \left( -\frac{r^2}{2R_{av}^L} \right). \quad (3.14)$$

753 The equation above assumes that  $R_{out}^L = R_{side}^L = R_{long}^L$  hence  $R_{av}^L = R_{out}^L$ . If this  
 754 condition is not satisfied, one can not give explicit mathematical relation between  
 755 one-dimensional and three-dimensional source sizes. However, for realistic val-  
 756 ues of  $R$  (i.e. for similar values of  $R_{out}$ ,  $R_{side}$ ,  $R_{long}$ ), the  $S_{3D}^{LCMS}$  from Eq. 3.13 is  
 757 not very different from Gaussian distribution and can be well approximated by  
 758 Eq. 3.13.

759 A deformation of an averaged source function in case of big differences in  
 760  $R_{out}$ ,  $R_{side}$ ,  $R_{long}$  is presented in the Fig. 3.3. A three-dimensional Gaussian dis-  
 761 tribution with varying widths was averaged into one-dimensional function using

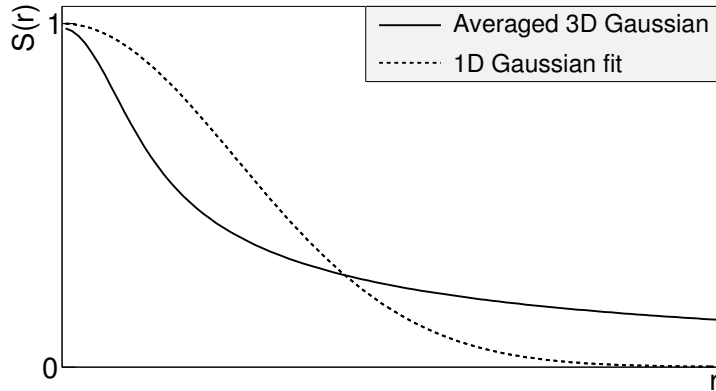


Figure 3.3: An averaged three-dimensional Gaussian source function with different widths was averaged into one-dimensional function. To illustrate deformations, one-dimensional Gaussian distribution was fitted.

the Eq. 3.13. Afterwards, an one-dimensional Gaussian distribution was fitted. One can notice a heavy tail of an averaged distribution in long  $r$  region, which makes an approximation using one-dimensional distribution in this case quite inaccurate.

Using Eq. 3.13 and Eq. 3.14 one can obtain a relation between one-dimensional width and the three-dimensional ones. Through numerical calculations one can find the following approximate relation [26]:

$$R_{av}^L = \sqrt{\left(R_{out}^{L^2} + R_{side}^{L^2} + R_{long}^{L^2}\right)/3}. \quad (3.15)$$

This equation does not depend on the pair velocity, hence it is valid in the LCMS and PRF.

### 3.2.4 Analytical form of a correlation function

The fundamental object in a particle interferometry is a correlation function. The correlation function is defined as:

$$C(\mathbf{p}_a, \mathbf{p}_b) = \frac{P_2(\mathbf{p}_a, \mathbf{p}_b)}{P_1(\mathbf{p}_a)P_1(\mathbf{p}_b)}, \quad (3.16)$$

where  $P_2$  is a conditional probability to observe a particle with momentum  $\mathbf{p}_b$  if particle with momentum  $\mathbf{p}_a$  was also observed. A  $P_1$  is a probability to observe a particle with a given momentum. The relationship between source emission function, pair wave function and the correlation function is described by the following equation:

$$C(\mathbf{p}_1, \mathbf{p}_2) = \int S_{AB}(\mathbf{p}_1, \mathbf{x}_1, \mathbf{p}_2, \mathbf{x}_2) |\Psi_{AB}|^2 d^4\mathbf{x}_1 d^4\mathbf{x}_2 \quad (3.17)$$

Substituting the one-dimensional emission function (Eq. 3.10) into the integral above yields the following form of correlation function in PRF:

$$C(q) = 1 + \lambda \exp(-R_{inv}^2 q^2) \quad (3.18)$$

where  $q$  is a momentum difference between two particles. When using the three-dimensional emission function (Eq. 3.11) one gets the following correlation function defined in the LCMS:

$$C(\mathbf{q}) = 1 + \lambda \exp(-R_{out}^2 q_{out}^2 - R_{side}^2 q_{side}^2 - R_{long}^2 q_{long}^2) \quad (3.19)$$

776 where  $q_{out}$ ,  $q_{side}$ ,  $q_{long}$  are  $\mathbf{q}$  components in the outward, sideward and longitudinal direction. The  $\lambda$  parameter in the equations above determines correlation  
 777 strength. The lambda parameter has values in the range  $\lambda \in [-0.5, 1]$  and it depends on a pair type. In case of pairs of identical bosons (like  $\pi\text{-}\pi$  or  $K\text{-}K$ ) the  
 778 lambda parameter  $\lambda \rightarrow 1$ . For identical fermions (e.g.  $p\text{-}p$ )  $\lambda \rightarrow -0.5$ . Values of  
 779  $\lambda$  observed experimentally are lower than 1 (for bosons) and greater than -0.5  
 780 (for fermions). There are few explanations to this effect: detector efficiencies,  
 781 inclusion of misidentified particles in a used sample or inclusion of non-correlated  
 782 pairs (when one or both particles come from e.g. long-lived resonance). The  
 783 analysis carried out in this work uses data from a model, therefore the detector  
 784 efficiency and particle purity is not taken into account [26].  
 785

### 786 3.2.5 Spherical harmonics decomposition of a correlation function

787 Results coming from an analysis using three-dimensional correlation function  
 788 in Cartesian coordinates are quite difficult to visualize. To do that, one usually  
 789 performs a projection into one dimension in outward, sideward and longitudinal  
 790 directions. One may loose important information about a correlation function in  
 791 this procedure, because it gives only a limited view of the full three-dimensional  
 792 structure. Recently, a more advanced way of presenting correlation function - a  
 793 spherical harmonics decomposition, was proposed. The three-dimensional cor-  
 794 relation function is decomposed into an infinite set of components in a form of  
 795 one-dimensional histograms  $C_l^m(q)$ . In this form, a correlation function is defined  
 796 as a sum of a series [27]:  
 797

$$C(\mathbf{q}) = \sum_{l,m} C_l^m(q) Y_l^m(\theta, \phi), \quad (3.20)$$

798 where  $Y_l^m(\theta, \phi)$  is a spherical harmonic function. Spherical harmonics are an  
 799 orthogonal set of solutions to the Laplace's equation in spherical coordinates  
 800 Hence, in this approach, a correlation function is defined as a function of  $q$ ,  $\theta$   
 801 and  $\phi$ . To obtain  $C_l^m$  coefficients in the series, one has to calculate the following  
 802 integral:

$$C_l^m(q) = \int_{\Omega} C(q, \theta, \phi) Y_l^{m*}(\theta, \phi) d\Omega, \quad (3.21)$$

803 where  $\Omega$  is a full solid angle.

Spherical harmonics representation has several important advantages. The main one is that it requires less statistics than traditional analysis performed in Cartesian coordinates. Another one is that it encodes full three-dimensional information in a set of one-dimensional plots. In principle it does not have to be an advantage, because full description of a correlation function requires infinite number of  $l, m$  components. But it so happens that the intrinsic symmetries of a pair distribution in a femtoscopic analysis result in most of the components to vanish. For the identical particles correlation functions, all coefficients with odd values of  $l$  and  $m$  disappear. It has also been shown, that the most significant portion of femtoscopic data is stored in the components with the lowest  $l$  values. It is expected that, the main femtoscopic information is contained in the following components [26]:

$$C_0^0 \rightarrow R_{LCMS}, \quad (3.22)$$

$$\Re C_2^0 \rightarrow \frac{R_T}{R_{long}}, \quad (3.23)$$

$$\Re C_2^2 \rightarrow \frac{R_{out}}{R_{side}}, \quad (3.24)$$

804 where  $R_{LCMS} = \sqrt{(R_{out}^2 + R_{side}^2 + R_{long}^2)/3}$  and  $R_T = \sqrt{(R_{out}^2 + R_{side}^2)/2}$ .  
 805 The  $C_0^0$  is sensitive to the overall size of a correlation function. The  $\Re C_2^0$  carries  
 806 the information about the ratio of the transverse to the longitudinal radii, due  
 807 to its  $\cos^2(\theta)$  weighting in  $Y_2^0$ . The component  $\Re C_2^2$  with its  $\cos^2(\phi)$  weighting  
 808 encodes the ratio between outward and sideward radii. Thus, the spherical har-  
 809 monics method allows to obtain and analyze full three-dimensional femtoscopic  
 810 information from a correlation function [26].

### 811 3.3 Experimental approach

812 The correlation function is defined as a probability to observe two particles  
 813 together divided by the product of probabilities to observe each of them sepa-  
 814 rately (Eq. 3.16). Experimentally this is achieved by dividing two distributions  
 815 of relative momentum of pairs of particles coming from the same event and the  
 816 equivalent distribution of pairs where each particle is taken from different colli-  
 817 sions. In this way, one obtains not only femtoscopic information but also all other  
 818 event-wide correlations. This method is useful for experimentalists to estimate  
 819 the magnitude of non-femtoscopic effects. There exists also a different approach,  
 820 where two particles in pairs in the second distribution are also taken from the  
 821 same event. The second method gives only information about physical effects  
 822 accessible via femtoscopy. The aim of this work is a study of effects coming from  
 823 two particle interferometry, hence the latter method was used.

824 In order to calculate experimental correlation function, one uses the follow-  
 825 ing approach. One has to construct two histograms: the *numerator*  $N$  and the

826 denominator  $D$  with the particle pairs momenta, where particles are coming from  
 827 the same event. Those histograms can be one-dimensional (as a function of  $|\mathbf{q}|$ ),  
 828 three dimensional (a function of three components of  $\mathbf{q}$  in LCMS) or a set of one-  
 829 dimensional histogram representing components of the spherical harmonic de-  
 830 composition of the distribution. The second histogram,  $D$  is filled for each pair  
 831 with the weight 1.0 at a corresponding relative momentum  $\mathbf{q} = 2\mathbf{k}^*$ . The first one,  
 832  $N$  is filled with the same procedure, but the weight is calculated as  $|\Psi_{ab}(\mathbf{r}^*, \mathbf{k}^*)|^2$ .  
 833 A division  $N/D$  gives the correlation function  $C$ . This procedure can be simply  
 834 written as [26]:

$$C(\mathbf{k}^*) = \frac{N}{D} = \frac{\sum_{n_i \in D} \delta(\mathbf{k}_i^* - \mathbf{k}^*) |\Psi_{ab}(\mathbf{r}_i^*, \mathbf{k}_i^*)|^2}{\sum_{n_i \in D} \delta(\mathbf{k}_i^* - \mathbf{k}^*)} . \quad (3.25)$$

The  $D$  histogram represents the set of all particle pairs used in calculations.  
 The  $n_i$  is a pair with the its relative momentum  $\mathbf{k}_i^*$  and relative separation  $\mathbf{r}_i^*$ .  
 Mathematically, the procedure of calculating the Eq. 3.25 is equivalent to a  
 calculation of an integral in Eq. 3.17 through a Monte-Carlo method. The wave  
 function used in Eq. 3.25 has one of the following forms:

$$|\Psi_{\pi\pi}(\mathbf{r}^*, \mathbf{k}^*)|^2 = |\Psi_{KK}(\mathbf{r}^*, \mathbf{k}^*)|^2 = 1 + \cos(2\mathbf{k}^* \mathbf{r}^*) , \quad (3.26)$$

$$|\Psi_{pp}(\mathbf{r}^*, \mathbf{k}^*)|^2 = 1 - \frac{1}{2} \cos(2\mathbf{k}^* \mathbf{r}^*) . \quad (3.27)$$

835 The first one is used in case of bosons, and the latter one is for identical fermions.  
 836 A wave function for pair of spin-1/2 fermions (Eq. 3.27) is a superposition of two  
 837 possible states: singlet state (with spin equal to 0 and one eigenstate) and triplet  
 838 state (with spin equal to 1 and three possible eigenstates). For a singlet state, a  
 839 wave function is symmetric, and for triplet state, it is antisymmetric. In other  
 840 words the  $|\Psi_{pp}|^2$  encodes correlation coming from Bose-Einstein statistics (with  
 841 weight 1/4) and anti-correlation from Fermi-Dirac distribution (with weight 3/4).

## 842 3.4 Scaling of femtoscopy radii

843 A particle interferometry formalism presented in the previous sections as-  
 844 sumes that particle emitting source is static. This is not the case in heavy ion  
 845 collisions at LHC. An existence of transverse radial and elliptic flow suggest that  
 846 created system is dynamic. To address this issue, a concept of *lengths of homogen-*  
 847 *eity* was introduced. It is defined as:

$$\frac{|f(p, x + \lambda) - f(p, x)|}{f(p, x)} = 1 , \quad (3.28)$$

848 where  $\lambda$  is the homogeneity length. It can be interpreted as the distance at which  
 849 relative change of the source Wigner function  $f$  becomes large. One can measure

the lengths of homogeneity of a system using femtoscopic radii. This concept can be intuitively explained on a basis of hydrodynamic models. Each source element is emitting particles with a velocity which is a combination of two components: a fluid cell velocity  $\beta_f$  (which is taken from the flow field  $u_\mu(x^\mu)$ ) and thermal velocity  $\beta_{th}$  (which has random direction). These particles can combine into pairs of small relative momenta and become correlated. If two particles are emitted far ( $|x_a - x_b| > \lambda$ ) away from each other, the flow field  $u_\mu$  in their point of emission might be very different and it will be impossible for them to have sufficiently small relative momenta to be in the region of interference effect. This effect is presented in Fig. 3.4. An increase of a correlation is visible for pairs with low relative momenta [8].

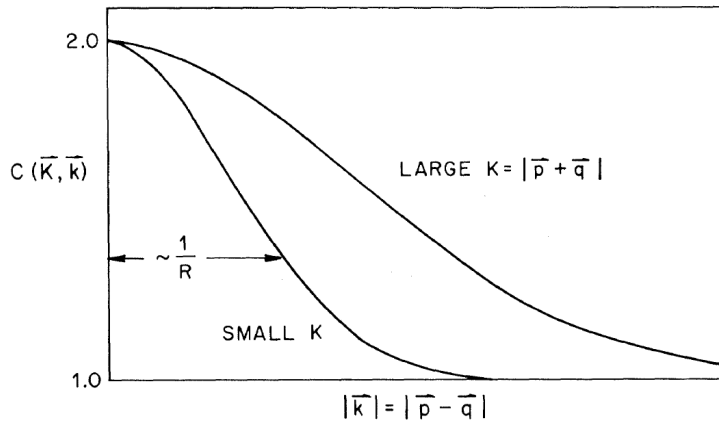


Figure 3.4: Correlation function width dependence on total pair momentum. Pion pairs with a large total momentum have a wider correlation (smaller apparent source) [28].

860

### 861 3.4.1 Scaling in LCMS

Hydrodynamic calculations performed in LCMS show that femtoscopic radii in outward, sideward, and longitudinal direction show dependence on transverse mass  $m_T = \sqrt{k_T^2 + m^2}$ , where  $m$  is a mass of a particle [29]. Moreover, experimental results show that this scaling is observed for  $R_{LCMS}$  radii also. This dependence can be expressed as follows:

$$R_i = \alpha m_T^{-\beta} \quad (3.29)$$

862 where  $i$  subscript indicates that this equation applies to  $R_{out}$ ,  $R_{side}$  and  $R_{long}$   
 863 radii. The  $\beta$  exponent is approximately equal 0.5. In case of strong transversal  
 864 expansion of the emitting source, the decrease of longitudinal interferometry ra-  
 865 dius can be more quick than  $m_T^{-0.5}$ , hence one can expect for longitudinal radii  
 866 greater values of  $\beta > 0.5$  [29].

### 3.4.2 Scaling in PRF

In the collisions at the LHC energies, pions are most abundant particles and their multiplicities are large enough to enable three-dimensional analysis. However, for heavier particles, such as kaons and protons statistical limitations arise. Hence it is often possible to only measure one-dimensional direction-averaged radius  $R_{inv}$  for those particles. The  $R_{inv}$  is then calculated in the PRF. The transition from LCMS to PRF is a Lorentz boost in the direction of pair transverse momentum with velocity  $\beta_T = p_T/m_T$ . Hence only  $R_{out}$  changes:

$$R_{out}^* = \gamma_T R_{out}. \quad (3.30)$$

A Lorentz factor  $\gamma_T = m_T/m$  depends on the particle type, therefore for the lighter particles (and for the same  $m_T$ )  $\gamma_T$  is much larger, which causes bigger growth of  $R_{out}$  and overall radius. This transformation to PRF breaks the scaling observed in the LCMS radii.

This increase of radius in the outward direction induces overall source size growth and whatsoever the source distribution function becomes non-gaussian. In this case the source function is developing long-range tails and its one-dimensional projection is much narrower than Gaussian distribution. This deformation is presented in Fig. 3.3. The influence of these effects can be expressed with an approximate formula:

$$R_{inv} = \sqrt{(R_{out}^2 \sqrt{\gamma_T} + R_{side}^2 + R_{long}^2)/3}. \quad (3.31)$$

Because the averaging of the radii is done in quadrature, one would have expected appearance of  $\gamma_T^2$  instead of  $\sqrt{\gamma_T}$  in this equation. However the Monte-Carlo procedure shows that this is not the case and the actual growth is smaller than the naive expectation. Numerical simulations yield that this increase is best described with the  $\sqrt{\gamma_T}$  in the Eq. 3.31 [30].

Assuming that radii in all directions are equal  $R_{out} = R_{side} = R_{long}$ , Eq. 3.31 can be reverted using Eq. 3.15 to express relationship between LCMS and PRF overall radii [30]:

$$R_{LCMS} \approx R_{inv} \times [(\sqrt{\gamma_T} + 2)/3]^{-1/2}. \quad (3.32)$$

This approximate formula allows to restore power-law behaviour of the scaled radii not only when the radii are equal, but also when their differences are small (for explanation see the last part of the Section 3.2.3).

This method of recovering scaling in PRF can be used as a tool for the search of hydrodynamic collectivity between pions, kaons and protons in heavy ion collisions with the measurement of one-dimensional radius in PRF.

896 **Chapter 4**

897 **Results**

898 For the purposes of the femtosopic analysis in this thesis, the THERMINATOR  
899 model was used to generate large number of events for eight different sets of  
900 initial conditions corresponding the following centrality ranges: 0-5%, 0-10%,  
901 10-20%, 20-30%, 30-40%, 40-50%, 50-60% and 60-70% for the Pb-Pb collisions at  
902 the centre of mass energy  $\sqrt{s_{NN}} = 2.76$  TeV. Software used in the process of  
903 calculating correlation functions is described in Appendix A. Plots in this chapter  
904 were generated using macros described in Appendix C.

905 **4.1 Identical particles correlations**

906 The correlation functions (three-dimensional and one-dimensional) were cal-  
907 culated separately for the following different pairs of identical particles:  $\pi$ - $\pi$ ,  $K$ -  
908  $K$  and  $p$ - $p$  for nine  $k_T$  bins (in GeV/c): 0.1-0.2, 0.2-0.3, 0.3-0.4, 0.4-0.5, 0.6-0.7,  
909 0.7-0.8, 0.8-1.0 and 1.0-1.2. In case of kaons,  $k_T$  ranges start from 0.3 and for pro-  
910 tons from 0.4 and for both of them the maximum value is 1.0. The  $k_T$  ranges for  
911 the heavier particles were limited to maintain sufficient multiplicity to perform  
912 reliable calculations.

913 **4.1.1 Spherical harmonics components**

914 The three-dimensional correlation function as a function of relative  
915 momentum  $q_{LCMS}$  was calculated in a form of components of spherical  
916 harmonics series accordingly to the Eq. 3.21. In the femtosopic analysis of  
917 identical particles, the most important information is stored in the  $\Re C_0^0$ ,  $\Re C_2^0$   
918 and  $\Re C_2^2$ , hence only those components were analyzed. Correlation functions  
919 obtained in this procedure were calculated for the different centrality bins for the  
920 pairs of pions, kaons and protons. They are presented in the Fig. 4.1, 4.2 and 4.3.

921 Coefficients for pairs of identical bosons (pions and kaons) are shown  
922 in the Fig. 4.1 and 4.2. The wave function symmetrization (Bose-Einstein  
923 statistics) causes the increase of a correlation in the low relative momenta

regime ( $q_{LCMS} < 0.06 \text{ GeV/c}$  or even  $q_{LCMS} < 0.12 \text{ GeV/c}$  for more peripheral collisions). It is clearly visible in the  $\Re C_0^0$  component. The  $\Re C_0^0$  resembles one-dimensional correlation function and in the sense that it encodes information about the overall source radius. The second coefficient  $\Re C_2^0$  differs from zero (is negative), which yields the information about the ratio  $R_T/R_{long}$ . The  $\Re C_2^2$  stores the information about  $R_{out}/R_{side}$  ratio and one can notice that it is non-vanishing (is also negative).

The correlation function for a pair of identical fermions is presented in the Fig. 4.3. A wave function for a pair of protons is a composition of singlet (described by Bose-Einstein statistics) and triplet state (described by the

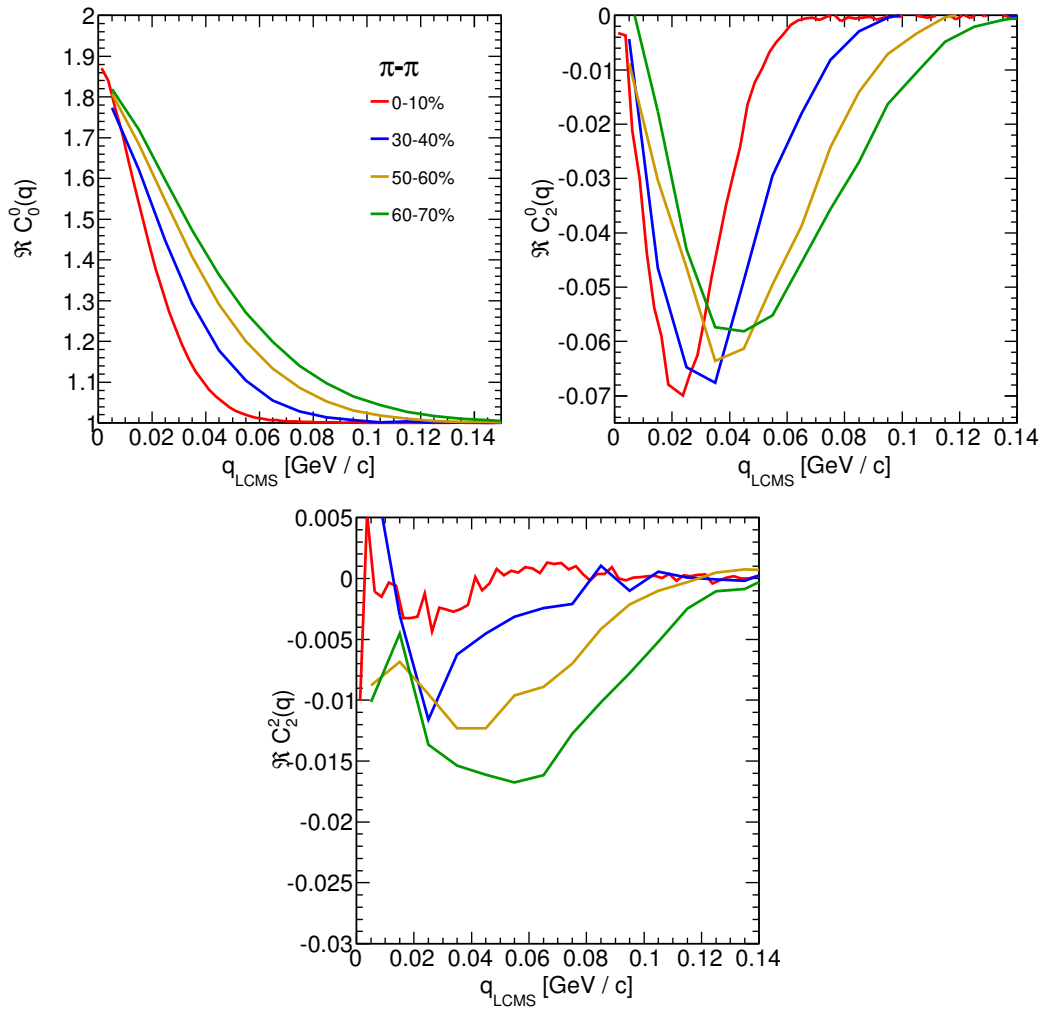


Figure 4.1: Spherical harmonics coefficients of the two-pion correlation function. From the top left:  $\Re C_0^0$ ,  $\Re C_2^0$  and  $\Re C_2^2$ . Only few centrality bins are presented for increased readability.

934 Fermi-Dirac statistics - see Section 3.3). An influence of Fermi-Dirac statistics has  
 935 its effect in the decrease of a correlation down to 0.5 at low relative momentum  
 936 ( $q_{LCMS} < 0.1 \text{ GeV/c}$  or  $q_{LCMS} < 0.15 \text{ GeV/c}$  for more peripheral collisions),  
 937 which can be observed in  $\Re C_0^0$ . The  $\Re C_2^0$  and  $\Re C_2^2$  coefficients differ from zero  
 938 and are becoming positive.

939 The common effect of the spherical harmonics form of a correlation function  
 940 is the "mirroring" of the shape of the  $\Re C_0^0$  coefficient - when correlation func-  
 941 tion increases at low  $q_{LCMS}$ , the  $\Re C_2^0$  and  $\Re C_2^2$  are becoming negative and vice  
 942 versa. This is quite different behaviour than in the case of correlations of non-

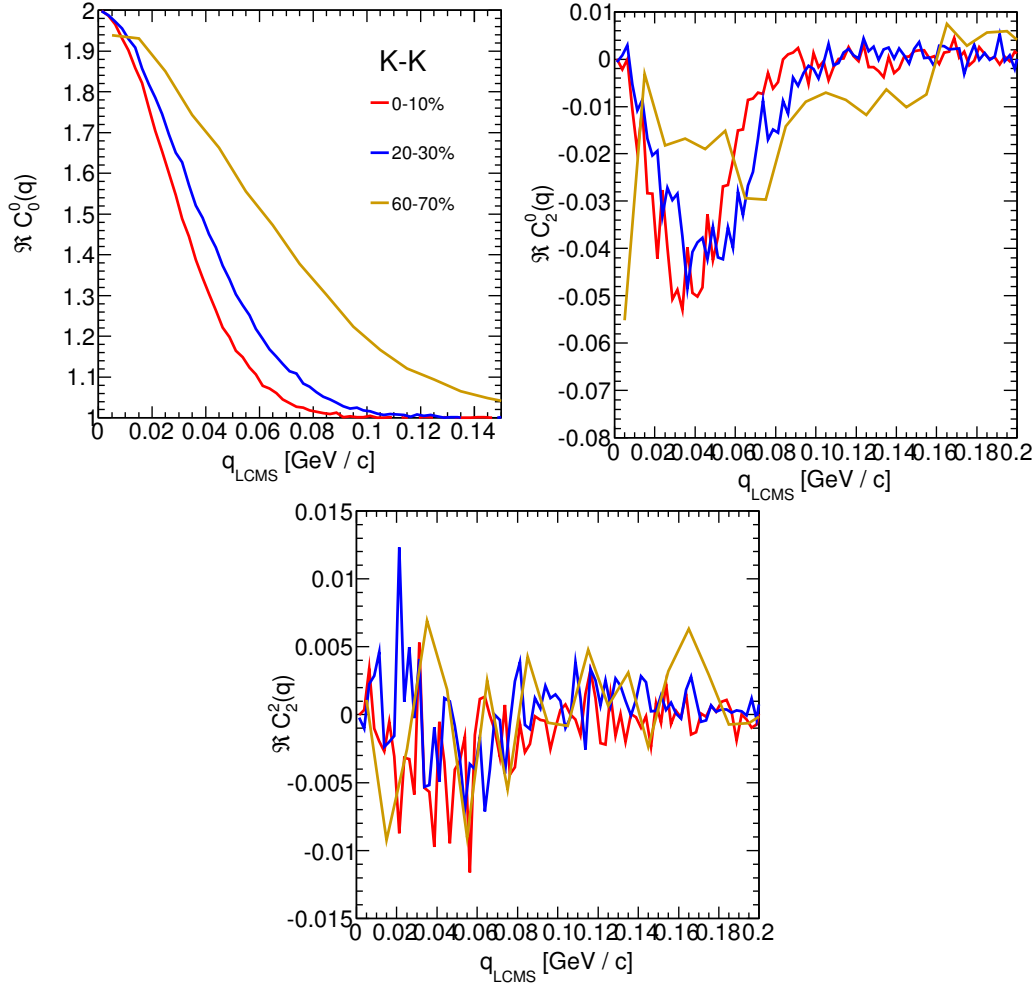


Figure 4.2: Spherical harmonics coefficients of the two-kaon correlation function. From the top left:  $\Re C_0^0$ ,  $\Re C_2^0$  and  $\Re C_2^2$ . Only few centrality bins are presented for increased readability. The  $\Re C_2^2$  is noisy, but one can still notice that it differs from zero and is becoming negative.

943 identical particles, where the  $\Re C_2^0$  still behaves in the same manner, but  $\Re C_2^2$  has  
 944 the opposite sign to the  $\Re C_2^0$  [26].

945 In all cases, the correlation function gets wider with the peripherality of a  
 946 collision i.e. the correlation function for most central collisions (0-10%) is much  
 947 narrower than for the most peripheral ones (60-70%). This phenomena in clearly  
 948 visible the  $\Re C_0^0$  coefficients. Other components are also affected by this effect,  
 949 this is especially noticeable in the case of kaons and pions. For the protons, the  
 950 results are noisy, hence this effect is not clearly distinguishable.

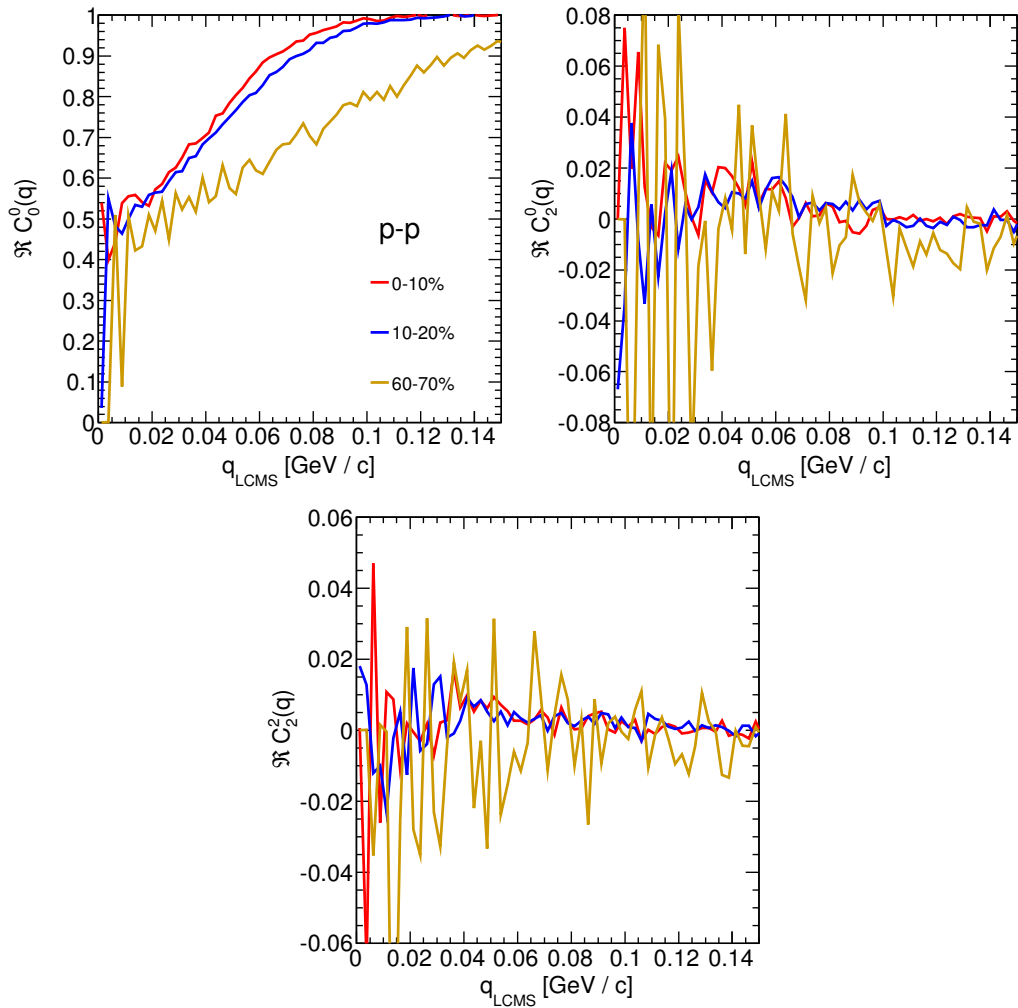
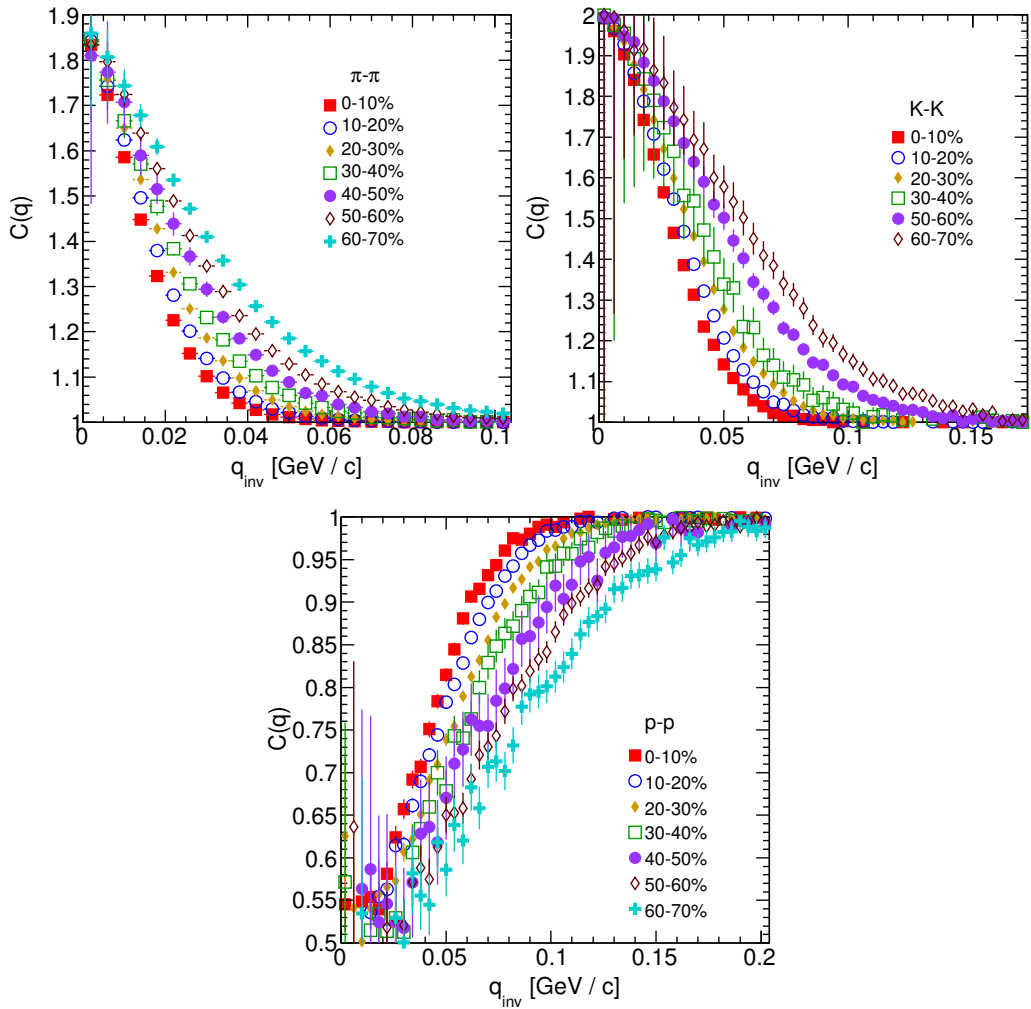


Figure 4.3: Spherical harmonics coefficients of the two-proton correlation function. From the top left:  $\Re C_0^0$ ,  $\Re C_2^0$  and  $\Re C_2^2$ . Only few centrality bins are presented for increased readability. The  $\Re C_2^0$  and  $\Re C_2^2$  are noisy, but one can still notice, that they differ from zero and are becoming positive.

951 **4.1.2 Centrality dependence of a correlation function**

952 The centrality dependence of a correlation function is especially visible in  
953 one-dimensional correlation functions. This effect is presented in the Fig. 4.4 -  
954 the correlation functions for pions, kaons and protons are plotted for the same  
955  $k_T$  range but different centrality bins. One can notice that the width of a func-  
956 tion is smaller in the case of most central collisions. Hence, the femtoscopic radii  
957 (proportional to the inverse of width) are increasing with the centrality. An ex-  
958 planation for this growth is that in the most central collisions, a size of a created  
959 system is larger than for the peripheral ones.



959 Figure 4.4: One-dimensional correlation function for pions (top left), kaons (top right) and protons (bottom) for different centralities.

### 4.1.3 $k_T$ dependence of a correlation function

In the Fig. 4.5 there are presented one-dimensional correlation functions for pions, kaons and protons for the same centrality bin, but different  $k_T$  ranges. One can observe in all cases of the particle types, appearance of the same trend: with the increase of the total transverse momentum of a pair, the width of a correlation function increases and the femtoscopic radius decreases. The plots in the Fig. 4.5 were zoomed in to show the influence of  $k_T$ .

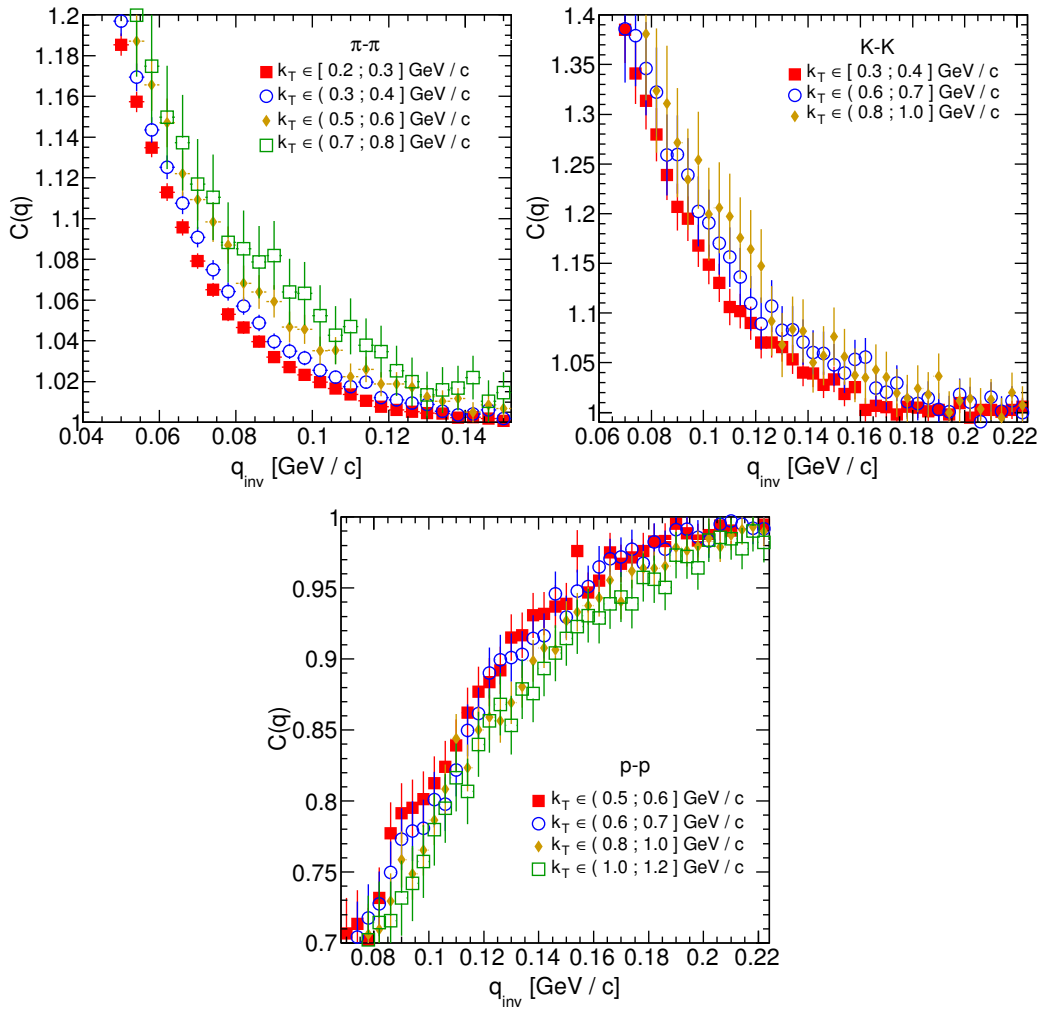


Figure 4.5: One-dimensional correlation functions for pions, kaons and protons, for the same centrality bin and different  $k_T$  ranges. The plot was zoomed in to the region which illustrates the  $k_T$  dependence in the best way. Only few of the calculated ranges are presented for better readability.

## 4.2 Results of the fitting procedure

In order to perform a quantitative analysis of a wide range of correlation functions, the theoretical formulas were fitted to the calculated experimental-like data. In this procedure, the femtoscopic radii for the three-dimensional as well as one-dimensional correlation functions were extracted. The main goal of this analysis is a verification of a common transverse mass scaling for different particles types. Obtained radii are plotted as a function of a transverse mass  $m_T = \sqrt{k_T^2 + m^2}$ . To test the scaling, the following power-law was fitted to the particular radii afterwards:

$$R_x = \alpha m_T^{-\beta}, \quad (4.1)$$

where the  $\alpha$  and  $\beta$  are free parameters. The procedure of fitting and used software are described in Appendix B.

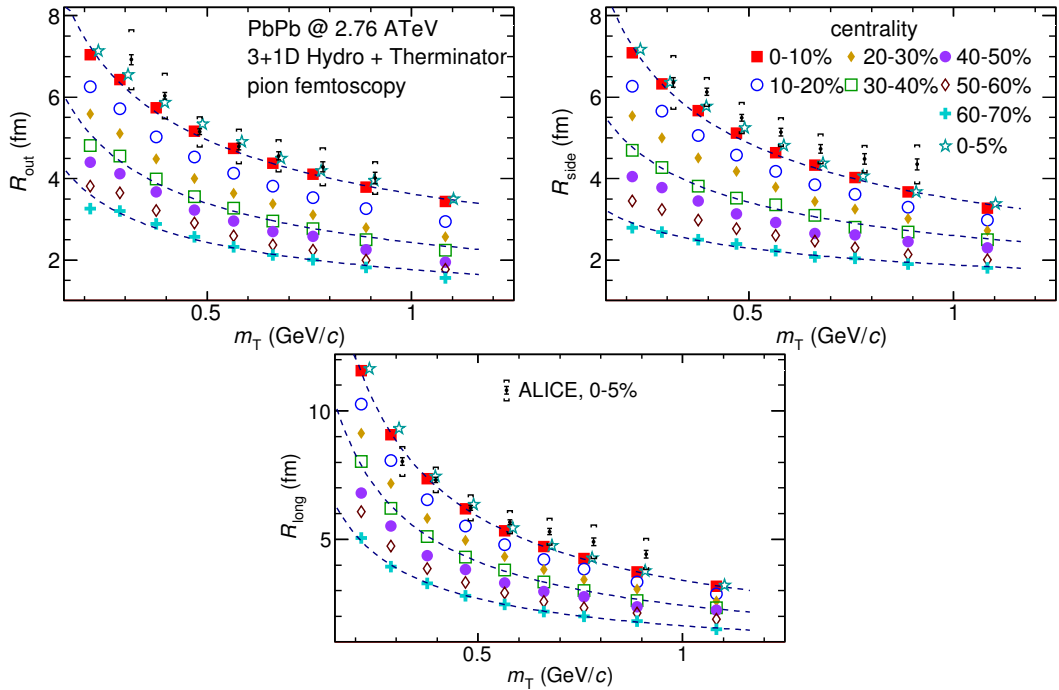


Figure 4.6: Femtoscopic radii in LCMS coming from two-pion correlation functions for all centrality bins as a function of  $m_T$ . The dashed lines are power-law fits. The most central collisions (0-5%) are compared to the results from ALICE [31]. The two datasets are shifted to the right for visibility [30].

### 4.2.1 The three-dimensional femtoscopic radii scaling

The femtoscopic radii in the outward, sideward and longitudinal directions for the analysis of two-pion correlation functions in the LCMS are presented in Fig. 4.6. The dashed lines are fits of the power law to the data. One can notice, that the power law describes data points well with a 5% accuracy. The  $\beta$  fit parameter for the outward direction is in the order of 0.45. For the sideward direction, this parameter has the similar value, but it is lower for the most peripheral collisions. In case of the longitudinal direction, the  $\beta$  has greater value, up to 0.75. In the Fig. 4.6, results for the top 5% central collisions (star-shaped markers) with experimental data from ALICE [31] are also compared. The experimental results are consistent with the ones coming from the model predictions.

The Fig. 4.7 presents femtoscopic radii coming from the kaon calculations. The  $R_{out}$ ,  $R_{side}$  and  $R_{long}$  fall also with the power-law within the 5% accuracy. The  $\beta$  parameter was larger in case of kaons: 0.59 in outward direction, 0.54 in the sideward and 0.86 for longitudinal.

The results for two-proton analysis are shown in the Fig. 4.8. The Eq. 4.1 was fitted to the data and tells that the protons also follow the  $m_T$  scaling within 5% range. The  $\beta$  parameter values were even bigger for the outward ( 0.58 ),

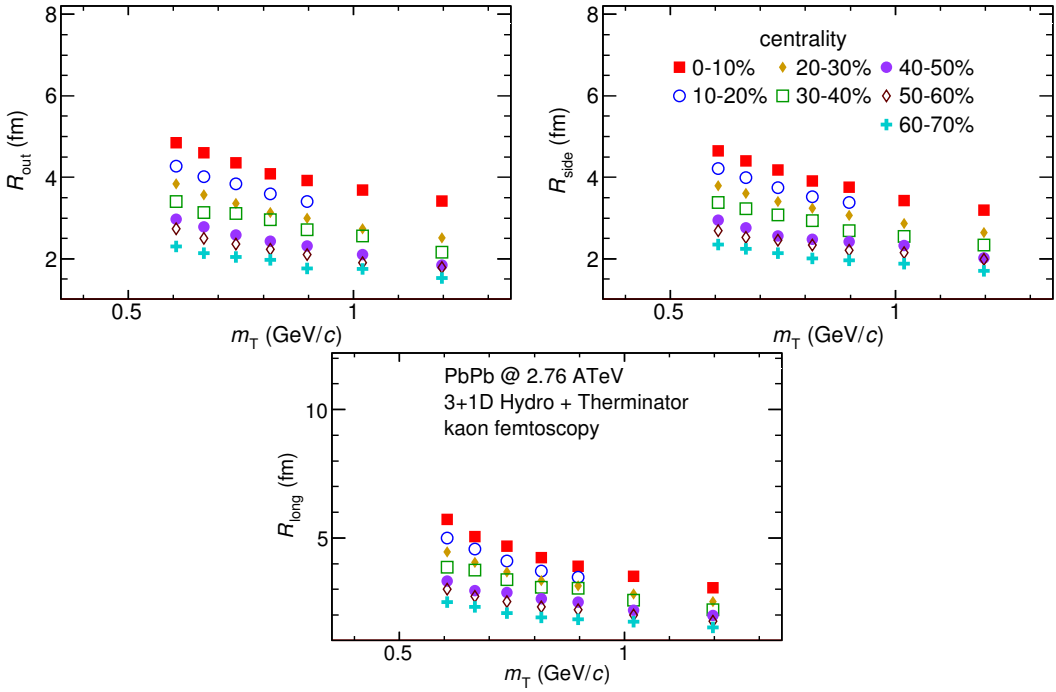


Figure 4.7: Femtoscopic radii extracted from two-kaon correlation functions for different centrality bins as a function of  $m_T$ . [30].

997 sideward ( 0.61 ) and longitudinal ( 1.09 ) directions than for the other particle  
 998 types.

999 The Fig. 4.9 presents results for the pions, kaons and protons together as a  
 1000 function of  $m_T$ . Considering differences in the  $\beta$  value for the fits for differ-  
 1001 ent particles, one can suspect that there is no common scaling between different  
 1002 kinds of particles. However, when all of the results shown on the same plot, they  
 1003 are aligning on the common curve and the scaling is well preserved. The scaling  
 1004 accuracy is 3%, 5% and 4% for the 0-10%, 20-30% and 60-70% for the outward  
 1005 direction. For the sideward radii the scaling is better, with average deviations  
 1006 2%, 2% and 3% respectively. In case of longitudinal direction the accuracy is 6%,  
 1007 5% and 3% for the three centralities. The  $\beta$  parameter for the outward direction is  
 1008 close to 0.42 in all cases. For the sideward direction it varies from 0.28 to 0.47 and  
 1009 is bigger for more central collisions. Regarding longitudinal radii, the exponent  
 1010 is bigger than the other two:  $\beta \in [0.62; 0.72]$  . Considering all results, the plotted  
 1011 radii are following the common power-law scaling within the 5% accuracy for all  
 1012 directions, centralities and particle types.

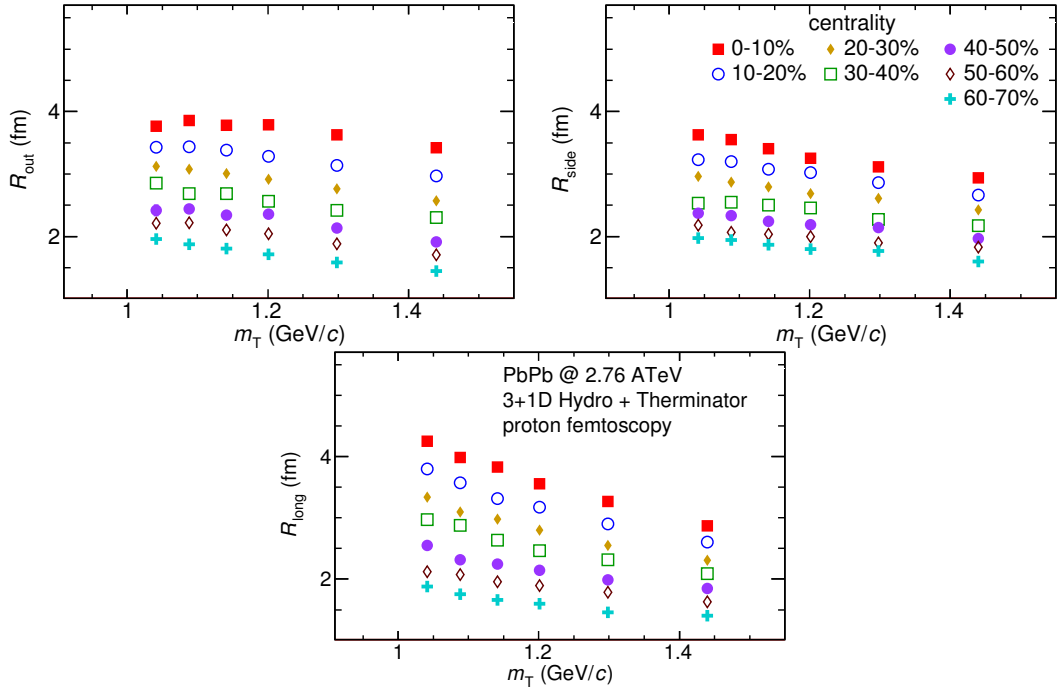


Figure 4.8: Femtoscopic radii extracted from two-proton correlation functions for different centrality bins as a function of  $m_T$ . [30].

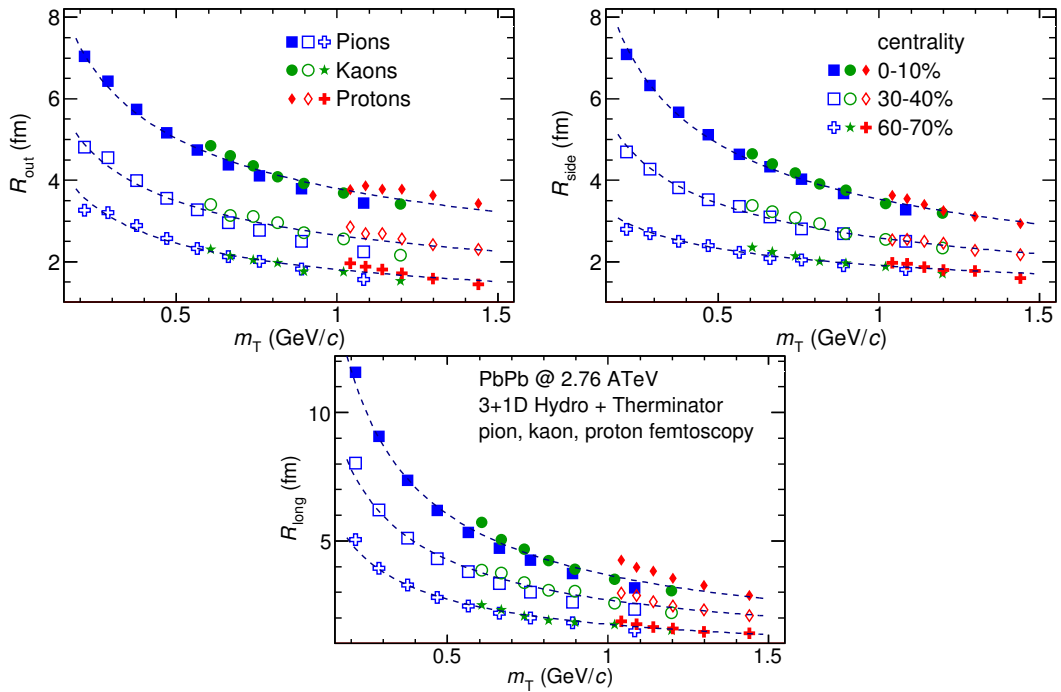


Figure 4.9: The results from the calculations for the pions, kaons and protons in for the three centralities presented on the common plot. One can notice that radii for particular centralities and different particle types follow the common power-law scaling. [30].

1013 **4.2.2 Scaling of one-dimensional radii**

1014 To the one-dimensional correlation function, the corresponding function in  
 1015 the PRF given by the Eq. 3.18 was fitted. The results from those fits are presented  
 1016 in the upper left plot in the Fig. 4.10. One immediately notices, that there is no  
 1017 common scaling of  $R_{inv}$  for different kind of particles. In Fig. 4.9 the radii in the  
 1018 outward direction for the pions, kaons and protons for the same  $m_T$  are similar.  
 1019 However, when one performs a transition from the LCMS to the PRF, the  $R_{out}$   
 1020 radius grows:

$$R_{out}^* = \gamma_T R_{out}, \quad (4.2)$$

1021 where  $\gamma_T = m_T/m$ . For the lighter particles, the  $\gamma_T$  is much larger, hence the  
 1022 bigger growth of the  $R_{out}$  and the overall radius. This is visible in the Fig. 4.10  
 1023 (top left), where the radii in the PRF for the lighter particles are bigger than for  
 1024 the heavier ones in case of the same  $m_T$  range.

1025 In the Fig. 4.9 there is visible scaling in the outward, sideward and longitudi-  
 1026 nal direction. Hence one can expect an appearance of such scaling in a direction-  
 1027 averaged radius calculated in the LCMS. This radius is presented in the Fig. 4.10  
 1028 (bottom) and indeed the  $R_{LCMS}$  exhibits power-law scaling with  $m_T$ .

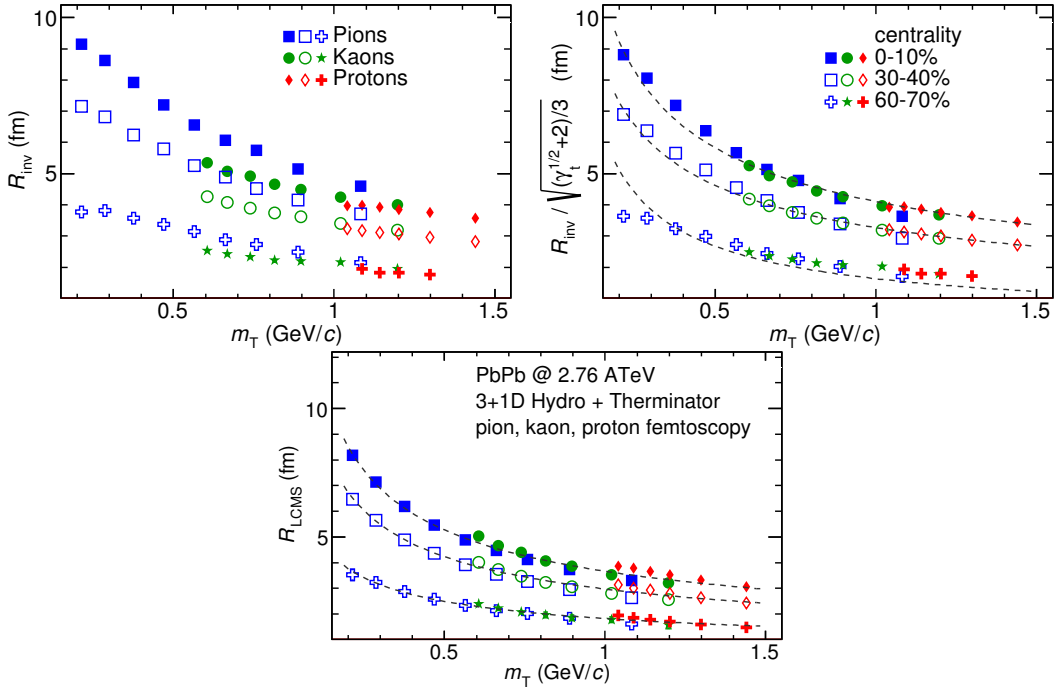


Figure 4.10: Top left: one-dimensional radius for pions, kaons and protons calculated in the PRF. Top right: the  $R_{inv}$  scaled by the proposed factor. Bottom: averaged one-dimensional radius in the LCMS for pions, kaons and protons. Only three centrality bins are shown for the better readability [30].

1029 One can try to account the effect of an increase of the radii in the outward direction  
 1030 by using the appropriate scaling factor. In Fig. 4.10 (top right), femtoscopic  
 1031 radii in the LCMS are divided by the proposed scaling factor:

$$f = \sqrt{(\sqrt{\gamma_T} + 2)/3} . \quad (4.3)$$

1032 The radii for pions, kaons and protons in the PRF after the division by  $f$  are  
 1033 following the power-law with the accuracy of 10%.

### 1034 4.3 Discussion of the results

1035 The femtoscopic radii obtained from the three-dimensional correlation func-  
 1036 tion fitting exhibit the  $m_T$  dependence described by the power law (Eq. 4.1). This  
 1037 scaling is preserved quite well with accuracy <10%. Observation of such scaling  
 1038 in a femtoscopic radii is a strong signal of the appearance of a collective beha-  
 1039 viour of a particle-emitting source created in the collision. The data used in the  
 1040 analysis was coming from the hydrodynamic model, hence one can indeed ex-  
 1041 pect the appearance of this scaling. However, the results for pion femtoscopy  
 1042 from the ALICE at LHC are consistent with the data from analysis performed in  
 1043 this thesis (Fig. 4.6). This is a confirmation of an applicability of hydrodynamic  
 1044 models in a description of an evolution of a quark-gluon plasma.

1045 The  $\beta$  parameter calculated in the fitting of the power-law to the femtoscopic  
 1046 radii is of the order of 0.5 in case of the radii in the transverse plane. This value is  
 1047 consistent with the hydrodynamic predictions. In case of longitudinal radii, the  
 1048 exponent is bigger (greater than 0.7), which is an indication of a strong transversal  
 1049 expansion in the system [29].

1050 A scaling described above is visible in the LCMS, however due to limited  
 1051 statistics, analysis in this reference frame is not always possible. In such case  
 1052 one performs calculations in the PRF. The  $m_T$  scaling in the PRF is not observed  
 1053 - this has a trivial kinematic origin. A transition from the PRF to LCMS causes  
 1054 growth of the radius in the outward direction and the common power-law scal-  
 1055 ing for different particles breaks due to differences in the  $\gamma_T(m_T)$  for different  
 1056 particle types. However one can try to deal with the radius growth and restore  
 1057 the scaling by dividing the radii  $R_{inv}$  by an approximate factor  $\sqrt{(\sqrt{\gamma_T} + 2)/3}$ .  
 1058 The scaled  $R_{inv}$  are following the power-law and could be used as a verification  
 1059 of hydrodynamic behaviour in the investigated particle source.

1060 The hadronic evolution and freeze-out in the THERMINATOR is followed by  
 1061 the resonance propagation and decay phase. A good accuracy of a scaling with  
 1062 the power-law indicated that the inclusion of the resonances does not break the  
 1063  $m_T$  scaling. However, recent calculations, which include also hadron rescatter-  
 1064 ing phase, indicate that the scaling between pions and kaons is broken at the  
 1065 LHC [32]. Thus, results from this work suggest that the scaling breaks at the  
 1066 hadron rescattering phase [30].

# Conclusions

This thesis presents the results of the two-particle femtoscopy of different particle kinds produced in Pb-Pb collisions at the centre of mass energy  $\sqrt{s_{NN}} = 2.76$  TeV. The analysed data was generated by the THERMINATOR model using the (3+1)-dimensional hydrodynamic model.

The momentum correlations were studied for three different types of particle pairs: pions, kaons and protons. The data was analyzed for eight different sets of initial conditions corresponding the following centrality ranges: 0-5%, 0-10%, 10-20%, 20-30%, 30-40%, 40-50%, 50-60% and 60-70%. The correlation functions were calculated for the nine  $k_T$  bins from 0.1 GeV/c to 1.2 GeV/c. The calculations were performed using spherical harmonics decomposition of a three-dimensional correlation function. Using this approach, one can obtain full three-dimensional information about the source size using only the three coefficients:  $\Re C_0^0$ ,  $\Re C_2^0$  and  $\Re C_2^2$ . To perform further quantitative analysis, the femtoscopic radii were extracted through fitting.

The calculated correlation functions show expected increase of a correlation at low relative momenta in case of identical bosons (pions and kaons) and the decrease for the identical fermions (protons) respectively. This effect is especially visible in the first spherical harmonic coefficient  $\Re C_0^0$ . The other two components  $\Re C_2^0$  and  $\Re C_2^2$  are non-vanishing and are providing information about the ratios of radii in the outward, sideward and longitudinal directions.

An increase of width of a correlation function with the peripherality of a collision and the  $k_T$  is observed for pions, kaons and protons. This increase of femtoscopic radii (proportional to the inverse of width) with the  $k_T$  is related with the  $m_T$  scaling predicted by the hydrodynamic calculations.

Hydrodynamic equations are predicting appearance of femtoscopic radii common scaling for different kinds of particles with the  $m_T^{-0.5}$  in the LCMS. In the results in this work, a common scaling for different particle types is observed in the LCMS in the outward, sideward and longitudinal direction. The direction-averaged radius  $R_{LCMS}$  also shows this power-law behaviour. The fitting of a power law  $\alpha m_T^{-\beta}$  to the femtoscopic radii yielded the information, that the  $\beta$  exponent for the outward and sideward direction is in order of 0.5, which is consistent with the hydrodynamic predictions. For the longitudinal direction, the  $\beta$  is bigger ( $>0.7$ ) than in the other directions which is an indication of a strong transverse flow. Femtoscopic radii in LCMS are following the

1102 power-law scaling with the accuracy <5% for pions and kaons, and <10% in case  
1103 of protons.

1104 In case of the one-dimensional radii  $R_{inv}$  calculated in the PRF, no common  
1105 scaling is observed. This is a consequence of a transition from the LCMS to the  
1106 PRF, which causes the growth of radius in the outward direction and breaks the  
1107 scaling for different particles. However, one can try to correct the influence of  
1108 the  $R_{out}$  growth with an approximate factor  $\sqrt{(\sqrt{\gamma_T} + 2)/3}$ . After the division  
1109 of the  $R_{inv}$  by the proposed factor, the scaling is restored with an accuracy <10%.  
1110 In this way, the experimentally simpler measure of the one-dimensional radii can  
1111 be used as a probe for the hydrodynamic collectivity.

1112 The THERMINATOR model includes hydrodynamic expansion, statistical had-  
1113 ronization, resonance propagation and decay afterwards. The  $m_T$  scaling is pre-  
1114 dicted from the pure hydrodynamic calculations. However, this study shows,  
1115 that influence of the resonances on this scaling is less than 10%.

1116 **Appendix A**

1117 **Scripts for correlation function  
1118 calculations**

1119 **A.1 Events generation**

1120 In order to perform analysis with sufficient statistics, a large amount of gen-  
1121 erated events was required. To handle this task of generation large amount of  
1122 data, a computer cluster at Faculty of Physics at Warsaw University of Techno-  
1123 logy was used. This cluster consists of 20 nodes with the following hardware  
1124 configuration: Intel® Core™ 2 Quad CPU Q6600 @ 2.40GHz, 8GB RAM with Sci-  
1125 entific Linux 5.8. The communication between nodes is realized by the TORQUE  
1126 Resource Manager [33]. To control process of launching multiple event gener-  
1127 ators and collecting the data, the following scripts were written using Bash script-  
1128 ing language:

1129 **skynet.sh** This is a script in a form of a batch job for TORQUE. It simply  
1130 launches multiple THERMINATOR processes in the same working directory  
1131 with the separate output directory for each job. This solution has two  
1132 advantages: saves space and computation time. A single freeze-out  
1133 hypersurface file has size about 230 MB and when running 20 instances  
1134 of generator this approach allows to avoid time- and space-consuming  
1135 copying of the whole THERMINATOR directory before running the  
1136 application. The second advantage is a sharing of files containing  
1137 information about particles' multiplicities and maximum integrands  
1138 between generator processes (more detailed description is in Section 2.3).  
1139 One can simply execute this batch job using the following command (an  
1140 example usage):

1141 `qsub -q long -t 0-19 skynet.sh -v dir=th_5.7,events=6000`  
1142 It adds 20 event generators (with task ids from 0 to 19) to the queue, sets  
1143 the THERMINATOR directory as `th_5.7` and sets a number of simulated  
1144 events to 6000 for each process. One has to execute this command in the  
1145 directory one level higher than `th_5.7` directory.

1146 **merge\_events.sh** After the generation process, one has to merge calculated  
 1147 events into one directory. This task requires renaming of a large number of  
 1148 THERMINATOR event files. Each event generator job produces files named  
 1149 with a certain pattern, starting from event000.root with increasing number.  
 1150 In order to move the event files and preserve continuity in the numbering,  
 1151 a simple script was written. An example of usage:  
 1152 

```
find /data/source -iname "event*.root" -type f \
  | merge_events.sh
```

  
 1153 This command will find all the event files in the directory /data/source,  
 1154 move and rename those files accordingly to the numeration of events in  
 1155 the current working directory.

1157 Sources of these two scripts are available on-line at [https://github.com/  
 1158 carbolymer/msc/tree/master/alix](https://github.com/carbolymer/msc/tree/master/alix).

## 1159 A.2 Calculations of experimental-like correlation 1160 functions

1161 Correlation functions used in this analysis were calculated using **tpi** soft-  
 1162 ware written by Adam Kisiel and was designed for reading event files from  
 1163 THERMINATOR. It uses ROOT library for calculations and storage of the data. The  
 1164 application provides functionality of calculation of one-dimensional correlation  
 1165 function in PRF, three-dimensional one in LCMS and its spherical harmonics de-  
 1166 composition (see Section 3.2.5). The exact numerical procedure of computation  
 1167 of a correlation function is presented in Section 3.3. **tpi** allows to perform calcu-  
 1168 lations with the following options:

- 1169 • Pair type - there are pion-pion, kaon-kaon, proton-proton and many more  
 1170 pairs available (including ones consisting of non-identical particles)
- 1171 • Multiple  $k_T$  subranges from 0.21 to 1.2 GeV/c
- 1172 • Possibility to include Coulomb interaction
- 1173 • Number of events to mix
- 1174 • Maximum freeze-out time
- 1175 • Choice of method of background calculation in correlation function (mixing  
 1176 events or using particles from the same event)

1177 This program generates results stored in the \*.root files in a form of histograms.  
 1178 Output file contains numerators, denominators and correlation functions from  
 1179 one-dimensional and three-dimensional analysis. Moreover, the spherical har-  
 1180 monics series coefficients up to  $l = 3$  with signal and background histograms are  
 1181 stored.

1182 **Appendix B**

1183 **Fitting utilities**

1184 Procedure of fitting analytical formulas to experimental-like correlation func-  
1185 tions was performed using custom software written in C++ and Bash. This ap-  
1186 plication utilizes MINUIT [34] package built in the ROOT library.

1187 **B.1 Minuit package**

1188 The MINUIT is a physics analysis tool for function minimization written in  
1189 Fortran programming language. This tool was designed for statistical analysis  
1190 and it is working on  $\chi^2$  or log-likelihood functions to compute the best-fit para-  
1191 meter values and uncertainties, including correlations between parameters. It is  
1192 implemented in ROOT environment as TMinuit class, which provides interface  
1193 to the minimization tool. The analysis performed in this work uses MINUIT with  
1194 the Migrad minimization method. The Migrad minimizer is the best one embed-  
1195 ded in Minuit. It's a variable-metric method with inexact line search, a stable  
1196 metric updating scheme, and checks for positive-definiteness [34].

1197 **B.2 Fitting software**

1198 Fitting utility provides tools for extraction of femtoscopic radii from correla-  
1199 tion functions for identical particles. It provides also a macro for generating plots  
1200 with these radii as a function of transverse mass and fitting power-law  $\alpha m_T^{-\beta}$  to  
1201 the results.

1202 **B.2.1 Input parameters**

1203 The application reads the output files from the tpi program and extracts  
1204 from them one-dimensional and three-dimensional correlation functions. The  
1205 latter ones are in a form of spherical harmonics series coefficients.

1206 One has also a possibility to set fit parameters for certain centrality bins, pair  
1207 types and  $k_T$  ranges. Configuration files (\*.conf) are located inside the applica-

tion's folder in the `data/` directory. Files with the names beginning with `fitsh` contain parameters for three-dimensional fits, while `fit1d` prefix indicates settings for one-dimensional ones. File `fitsh.kk.conf` contains initial parameters for all fits for pairs of kaons. Similarly, one can set fit parameters for pions (`pipi`) and protons (`pp`) using corresponding letters in place of `kk` in the name of the file.

Here is an example parameter file for one-dimensional fit (`fit1d`):

1.0	L	normalization
1.0	L	$\lambda$
4.0	L	$R_{inv}$
0.0	F	not used

The `F` letter after the parameter indicates that it is a fixed value (will not change during fitting process), whereas the `L` parameter tells that this value will be modified.

An example parameter file for three-dimensional fit (`fitsh`):

4.5	L	1.2	5.5	$R_{out}$ in fm
4.5	L	1.2	5.5	$R_{side}$ in fm
4.5	L	1.2	6.5	$R_{long}$ in fm
0.70	L	0.2	2.2	$\lambda$
1.14	F	1.14	1.14	$C_2^0$ coefficient
1.25	F	1.25	1.25	$C_2^2$ coefficient
1.0	L	0.8	1.2	overall normalization
0.0	F	0.0	0.0	$C_2^0$ normalization
0.0	F	0.0	0.0	$C_2^2$ normalization
0.25	F	0.25	0.25	$q_{beg}$
0.25	F	0.25	0.25	$q_{slope}$
0.0	F	0.0	0.0	not used
0.0	F	0.0	0.0	not used
0.0	F	0.0	0.0	not used
0.0	F	0.0	0.0	not used
0.0	F	0.0	0.0	not used
0.0	F	0.0	0.0	not used
0.0	F	0.0	0.0	not used
0.0	F	0.0	0.0	not used
IdLCY1m				correlation function numerator name
0.0075				beginning of the fitting range ( $q$ in GeV/c)
0.2				end of the fitting range ( $q$ in GeV/c)

0	not used

1218 This file contains extra columns indicating allowed range for value of a fit  
 1219 parameter. The first number (the 3rd column) is the minimum and the second  
 1220 one (4th column) is the maximum of this range.

### 1221 **B.2.2 Output format**

1222 The application during calculations creates inside `data/` directory, subdirectories  
 1223 for each centrality. For each pair type and each of the following variables  
 1224  $R_{inv}$ ,  $R_{out}$ ,  $R_{side}$ ,  $R_{long}$ ,  $\lambda$  and  $R_{LCMS}$ , the output files `*.out` with four columns are  
 1225 created. First column is the beginning of the  $k_T$  range, second one is the ending  
 1226 of the range, third column contains result of the fit and the last one stores un-  
 1227 certainty of this value. In addition, plots (in the png format) of the correlation  
 1228 functions for each pair type and  $k_T$  bin are generated inside subdirectories.

1229 Files `filelist.{pair type}.in` contain list of input `*.root` files with correlation func-  
 1230 tions, which were processed.

### 1231 **B.2.3 Compilation**

1232 This utility requires ROOT framework and `libboost-regex-dev` library.  
 1233 Compilation can be performed using `make` command inside application direct-  
 1234 ory.

### 1235 **B.2.4 Usage**

#### 1236 **Fitting process**

1237 In order to execute fitting process, one should execute the following com-  
 1238 mand:

1239 `./run.sh /path/to/the/tpi/output centrality`

1240 The `/path/to/the/tpi/output` parameter is a location of `tpi` output files  
 1241 and `centrality` is a name of a directory in which the output will be stored.

#### 1242 **Plotting**

1243 In order to plot femtoscopic radii and perform fitting of power law, one has  
 1244 to use the following command:

1245 `make plots`

1246 Plots will be generated in the output directory.

1247 The source of fitting software is available on-line at <https://github.com/carbolymer/msc/tree/master/fitting>.

<sub>1249</sub> **Appendix C**

<sub>1250</sub> **Plotting scripts**

# <sup>1251</sup> Bibliography

- <sup>1252</sup> [1] Standard Model of Elementary Paticles - Wikipedia, the free encyclopedia  
<sup>1253</sup> [http://en.wikipedia.org/wiki/Standard\\_Model](http://en.wikipedia.org/wiki/Standard_Model).
- <sup>1254</sup> [2] R. Aaij et al. (LHCb Collaboration). Observation of the resonant character of  
<sup>1255</sup> the  $z(4430)^-$  state. *Phys. Rev. Lett.*, 112:222002, Jun 2014.
- <sup>1256</sup> [3] Donald H. Perkins. *Introduction to High Energy Physics*. Cambridge University Press,  
<sup>1257</sup> fourth edition, 2000. Cambridge Books Online.
- <sup>1258</sup> [4] G. Odyniec. *Phase Diagram of Quantum Chromo-Dynamics* - course at Faculty  
<sup>1259</sup> of Physics, Warsaw University of Technology, Jun 2012.
- <sup>1260</sup> [5] J. Beringer et al. (Particle Data Group). The Review of Particle Physics. *Phys.*  
<sup>1261</sup> *Rev.*, D86:010001, 2012.
- <sup>1262</sup> [6] Z. Fodor and S.D. Katz. The Phase diagram of quantum chromodynamics.  
<sup>1263</sup> 2009.
- <sup>1264</sup> [7] F. Karsch. Lattice results on QCD thermodynamics. *Nuclear Physics A*, 698(1-  
<sup>1265</sup> 4):199 – 208, 2002.
- <sup>1266</sup> [8] Adam Kisiel. *Studies of non-identical meson-meson correlations at low relative ve-*  
<sup>1267</sup> *locities in relativistic heavy-ion collisions registered in the STAR experiment*. PhD  
<sup>1268</sup> thesis, Warsaw University of Technology, Aug 2004.
- <sup>1269</sup> [9] J. Bartke. *Relativistic Heavy Ion Physics*. World Scientific Pub., 2009.
- <sup>1270</sup> [10] W. Florkowski. *Phenomenology of Ultra-Relativistic Heavy-Ion Collisions*.  
<sup>1271</sup> World Scientific, 2010.
- <sup>1272</sup> [11] Science Grid This Week, October 25, 2006 - Probing the Perfect Liquid with  
<sup>1273</sup> the STAR Grid [http://www.interactions.org/sgtw/2006/1025/](http://www.interactions.org/sgtw/2006/1025/star_grid_more.html)  
<sup>1274</sup> [star\\_grid\\_more.html](http://www.interactions.org/sgtw/2006/1025/star_grid_more.html).
- <sup>1275</sup> [12] K. Grebieszkow. Fizyka zderzeń ciężkich jonów, <http://www.if.pw.edu.pl/~kperl/HIP/hip.html>.
- <sup>1277</sup> [13] Ulrich W. Heinz. From SPS to RHIC: Maurice and the CERN heavy-ion  
<sup>1278</sup> programme. *Phys.Scripta*, 78:028005, 2008.

- 1279 [14] J. Adams et al. Identified particle distributions in pp and Au+Au collisions  
1280 at  $s_{\text{NN}}^{**}(1/2) = 200 \text{ GeV}$ . *Phys.Rev.Lett.*, 92:112301, 2004.
- 1281 [15] G. David, R. Rapp, and Z. Xu. Electromagnetic Probes at RHIC-II. *Phys.Rept.*,  
1282 462:176–217, 2008.
- 1283 [16] A. Marin et al. Dilepton measurements with CERES. *PoS*, CPOD07:034,  
1284 2007.
- 1285 [17] J. Adams et al. Experimental and theoretical challenges in the search for the  
1286 quark gluon plasma: The STAR Collaboration’s critical assessment of the  
1287 evidence from RHIC collisions. *Nucl.Phys.*, A757:102–183, 2005.
- 1288 [18] Adam Kisiel, Tomasz Taluc, Wojciech Broniowski, and Wojciech  
1289 Florkowski. THERMINATOR: THERMal heavy-IoN generATOR. *Comput.Phys.Commun.*, 174:669–687, 2006.
- 1291 [19] Mikolaj Chojnacki, Adam Kisiel, Wojciech Florkowski, and Wojciech Bro-  
1292 niowski. THERMINATOR 2: THERMal heavy IoN generATOR 2. *Comput.  
1293 Phys.Commun.*, 183:746–773, 2012.
- 1294 [20] ROOT - A Data Analysis Framework <http://root.cern.ch/drupal/>.
- 1295 [21] I. et al (BRAHMS Collaboration) Bearden. Charged meson rapidity distri-  
1296 butions in central Au + Au collisions at  $\sqrt{s_{\text{NN}}} = 200 \text{ GeV}$ . *Phys. Rev. Lett.*,  
1297 94:162301, Apr 2005.
- 1298 [22] W. Israel and J.M. Stewart. Transient relativistic thermodynamics and kin-  
1299 etic theory. *Annals of Physics*, 118(2):341 – 372, 1979.
- 1300 [23] Piotr Bożek. Flow and interferometry in (3 + 1)-dimensional viscous hydro-  
1301 dynamics. *Phys. Rev. C*, 85:034901, Mar 2012.
- 1302 [24] K. Kovtun, P. D. T. Son, and A. O. Starinets. Viscosity in strongly interacting  
1303 quantum field theories from black hole physics. *Phys. Rev. Lett.*, 94:111601,  
1304 Mar 2005.
- 1305 [25] Fred Cooper and Graham Frye. Single-particle distribution in the hydro-  
1306 dynamic and statistical thermodynamic models of multiparticle production.  
1307 *Phys. Rev. D*, 10:186–189, Jul 1974.
- 1308 [26] Adam Kisiel. Nonidentical-particle femtoscopy at  $\sqrt{s_{\text{NN}}} = 200 \text{ GeV}$  in hy-  
1309 drodynamics with statistical hadronization. *Phys. Rev. C*, 81:064906, Jun  
1310 2010.
- 1311 [27] Adam Kisiel and David A. Brown. Efficient and robust calculation of femto-  
1312 scopic correlation functions in spherical harmonics directly from the raw  
1313 pairs measured in heavy-ion collisions. *Phys.Rev.*, C80:064911, 2009.

- 1314 [28] S. Pratt. Pion Interferometry for Exploding Sources. *Phys.Rev.Lett.*, 53:1219–  
1315 1221, 1984.
- 1316 [29] S.V. Akkelin and Yu.M. Sinyukov. The HBT-interferometry of expanding  
1317 inhomogeneous sources. *Z.Phys.*, C72:501–507, 1996.
- 1318 [30] A. Kisiel, M. Galazyn, and P. Bozek. Pion, kaon, and proton femtoscopy in  
1319 Pb–Pb collisions at  $\sqrt{s_{NN}}=2.76$  TeV modeled in 3+1D hydrodynamics. 2014.
- 1320 [31] K. Aamodt et al. Two-pion Bose-Einstein correlations in central Pb-Pb colli-  
1321 sions at  $\sqrt{s_{NN}} = 2.76$  TeV. *Phys.Lett.*, B696:328–337, 2011.
- 1322 [32] V.M. Shapoval, P. Braun-Munzinger, Iu.A. Karpenko, and Yu.M. Sinyukov.  
1323 Femtoscopy correlations of kaons in  $Pb + Pb$  collisions at LHC within hy-  
1324 drokinetic model. 2014.
- 1325 [33] TORQUE Resource Manager - An open source resource manager provid-  
1326 ing control over batch jobs and distributed compute nodes <http://www.adaptivecomputing.com/products/open-source/torque/>.
- 1327 [34] MINUIT - Function Minimization and Error Analysis <http://wwwasdoc.web.cern.ch/wwwasdoc/minuit/minmain.html>.

# List of Figures

1.1	The Standard Model of elementary particles [1]. . . . .	3
1.2	A string breaking and a creation of a new quark-anti-quark pair [4]. . . . .	5
1.3	The coupling parameter $\alpha_s$ dependence on four-momentum transfer $Q^2$ [5]. . . . .	6
1.4	The QCD potential for a quark-antiquark pair as a function of distance for different temperatures. A value of a potential decreases with the temperature [4]. . . . .	7
1.5	A number of degrees of freedom as a function of a temperature [7]. . . . .	7
1.6	Phase diagram coming from the Lattice QCD calculations [8]. . . . .	8
1.7	Left: stages of a heavy ion collision simulated in the UrQMD model. Right: schematic view of a heavy ion collision evolution [8]. . . . .	9
1.8	Overlapping region which is created in heavy ion collisions has an almond shape. Visible x-z plane is a <i>reaction plane</i> . The x-y plane is a <i>transverse plane</i> . The z is a direction of the beam [11]. . . . .	11
1.9	Cross-section of a heavy ion collision in a transverse plane. The $b$ parameter is an <i>impact parameter</i> - a distance between centers of nuclei during a collision. An impact parameter is related with the centrality of a collision and a volume of the quark-gluon plasma [12]. . . . .	12
1.10	<i>Lower:</i> The elliptic flow $v_2$ follows the hydrodynamical predictions for an ideal fluid perfectly. Note that > 99% of all final hadrons have $p_T < 1.5 \text{ GeV}/c$ . <i>Upper left:</i> The $v_2$ plotted versus transverse kinetic energy $KE_T = m_T - m_0 = \sqrt{p_T^2 + m_0^2} - m_0$ . The $v_2$ follows different universal curves for mesons and baryons. <i>Upper right:</i> When scaled by the number of valence quarks, the $v_2$ follows the same universal curve for all hadrons and for all values of scaled transverse kinetic energy [13]. . . . .	13
1.11	Invariant yield of particles versus transverse mass $m_T = \sqrt{p_T^2 + m_0^2}$ for $\pi^\pm$ , $K^\pm$ , $p$ and $\bar{p}$ at mid-rapidity for p+p collisions (bottom) and Au+Au events from 70-80% (second bottom) to 0-5% (top) centrality [14]. . . . .	14

1361	1.12 Thermal photons spectra for the central Au+Au collisions at				
1362	$\sqrt{s_{NN}} = 200$ GeV computed within different hydrodynamical				
1363	models compared with the pQCD calculations (solid line) and				
1364	experimental data from PHENIX (black dots) [15]. . . . .	15			
1365	1.13 Left: Invariant mass spectrum of $e^+e^-$ pairs in Pb+Au collisions				
1366	at 158A GeV compared to the sum coming from the hadron decays				
1367	predictions. Right: The expectations coming from model calcula-				
1368	tions assuming a dropping of the $\rho$ mass (blue) or a spread of the				
1369	$\rho$ width in the medium (red) [16]. . . . .	16			
1370	1.14 Azimuthal angle difference $\Delta\phi$ distributions for different colliding				
1371	systems at $\sqrt{s_{NN}} = 200$ GeV. Transverse momentum cut: $p_T > 2$				
1372	GeV. For the Au+Au collisions the away-side jet is missing [17]. . .	17			
1373	2.1 The cascade decay in the single freeze-out model. An unstable res-				
1374	onance $x_N$ is formed at the freeze-out hypersurface and travels for				
1375	the time $\tau_N$ depending on its lifetime and decays. If the products				
1376	are also resonances ( $x_{N-1}$ , $x_2$ ) they decay further until the stable				
1377	particles are formed ( $x_1$ ) [18]. . . . .	24			
1378	3.1 Bertsch-Pratt direction naming convention used in heavy ion col-				
1379	lision. . . . .	26			
1380	3.2 The pair wave function is a superposition of all possible states. In				
1381	case of particle interferometry it includes two cases: particles with				
1382	momenta $p_1, p_2$ registered by detectors $A, B$ and $p_1, p_2$ registered				
1383	by $B, A$ respectively. . . . .	27			
1384	3.3 An averaged three-dimensional Gaussian source function with dif-				
1385	ferent widths was averaged into one-dimensional function. To il-				
1386	lustrate deformations, one-dimensional Gaussian distribution was				
1387	fitted. . . . .	30			
1388	3.4 Correlation function width dependence on total pair momentum.				
1389	Pion pairs with a large total momentum have a wider correlation				
1390	(smaller apparent source) [28]. . . . .	34			
1391	4.1 Spherical harmonics coefficients of the two-pion correlation func-				
1392	tion. From the top left: $\Re C_0^0$ , $\Re C_2^0$ and $\Re C_2^2$ . Only few centrality				
1393	bins are presented for increased readability. . . . .	37			
1394	4.2 Spherical harmonics coefficients of the two-kaon correlation func-				
1395	tion. From the top left: $\Re C_0^0$ , $\Re C_2^0$ and $\Re C_2^2$ . Only few centrality				
1396	bins are presented for increased readability. The $\Re C_2^2$ is noisy, but				
1397	one can still notice that it differs from zero and is becoming negative. .	38			

1398	4.3 Spherical harmonics coefficients of the two-proton correlation function. From the top left: $\Re C_0^0$ , $\Re C_2^0$ and $\Re C_2^2$ . Only few centrality bins are presented for increased readability. The $\Re C_2^0$ and $\Re C_2^2$ are noisy, but one can still notice, that they differ from zero and are becoming positive. . . . .	39
1399		
1400		
1401		
1402		
1403	4.4 One-dimensional correlation function for pions (top left), kaons (top right) and protons (bottom) for different centralities. . . . .	40
1404		
1405		
1406		
1407	4.5 One-dimensional correlation functions for pions, kaons and protons, for the same centrality bin and different $k_T$ ranges. The plot was zoomed in to the region which illustrates the $k_T$ dependence in the best way. Only few of the calculated ranges are presented for better readability. . . . .	41
1408		
1409		
1410	4.6 Femtoscopic radii in LCMS coming from two-pion correlation functions for all centrality bins as a function of $m_T$ . The dashed lines are power-law fits. The most central collisions (0-5%) are compared to the results from ALICE [31]. The two datasets are shifted to the right for visibility [30]. . . . .	42
1411		
1412		
1413		
1414		
1415	4.7 Femtoscopic radii extracted from two-kaon correlation functions for different centrality bins as a function of $m_T$ . [30]. . . . .	43
1416		
1417	4.8 Femtoscopic radii extracted from two-proton correlation functions for different centrality bins as a function of $m_T$ . [30]. . . . .	44
1418		
1419	4.9 The results from the calculations for the pions, kaons and protons in for the three centralities presented on the common plot. One can notice that radii for particular centralities and different particle types follow the common power-law scaling. [30]. . . . .	45
1420		
1421		
1422		
1423	4.10 Top left: one-dimensional radius for pions, kaons and protons calculated in the PRF. Top right: the $R_{inv}$ scaled by the proposed factor. Bottom: averaged one-dimensional radius in the LCMS for pions, kaons and protons. Only three centrality bins are shown for the better readability [30]. . . . .	46
1424		
1425		
1426		
1427		